Graphene/semiconductor nanocomposites (GSNs) for heterogeneous photocatalytic decolorization of wastewaters contaminated with synthetic dyes: A review

ARTICLE *in* APPLIED CATALYSIS B ENVIRONMENTAL · NOVEMBER 2014

Impact Factor: 7.44 · DOI: 10.1016/j.apcatb.2014.05.035

2 AUTHORS:

Shamik Chowdhury
National University of Singapore
11 PUBLICATIONS **81** CITATIONS
SEE PROFILE

Rajasekhar Balasubramanian
National University of Singapore
235 PUBLICATIONS **3,227** CITATIONS
SEE PROFILE

Applied Catalysis B: Environmental 160–161 (2014) 307–324

Contents lists available at ScienceDirect

Applied Catalysis B: Environmental

journal homepage: www.elsevier.com/locate/apcatb

Graphene/semiconductor nanocomposites (GSNs) for heterogeneous photocatalytic decolorization of wastewaters contaminated with synthetic dyes: A review

Shamik Chowdhury, Rajasekhar Balasubramanian*

Department of Civil and Environmental Engineering, National University of Singapore, 1 Engineering Drive 2, Singapore 117576, Republic of Singapore

ARTICLE INFO

Article history:
Received 25 December 2013
Received in revised form 11 May 2014
Accepted 20 May 2014
Available online 29 May 2014

Keywords:
Dyes
Graphene nanocomposites
Heterogeneous photocatalysis
Photocatalyst
Semiconductors

ABSTRACT

The advent of graphene revolution in recent years has opened up immense possibilities for creating and exploring new carbon-based materials for innovative technological applications. Recent advancements have shown that graphene/semiconductor nanocomposites (GSNs) can be envisaged as a promising new class of catalysts for the heterogeneous photocatalytic treatment of industrial wastewaters. While GSNs have been found effective in degrading and mineralizing a myriad of organic contaminants, photocatalytic degradation of synthetic colorants has been most extensively investigated. We present here the state-of-art review on GSNs in the context of photodecolorization of textile effluents. Various approaches to the synthesis of GSNs are first integrated and demonstrated by representative examples. The efficacy of these composite photocatalysts in decomposing selected dye pollutants is then discussed. We conclude the review by emphasizing the future research challenges and opportunities toward the large-scale commercialization of GSNs.

1. Introduction

The rapid pace of industrialization has largely contributed to the severe deterioration of our freshwater resources. A wide range of toxic and hazardous substances are continually being released into the surrounding water bodies due to lack of effective effluent treatment at the source, among which synthetic dyes have attracted considerable attention. Worldwide, 280,000 t of synthetic dyes have been estimated to be released into the environment every year through industrial wastewater discharges [1]. Dyes are tinctorially strong and hence easily visible in contaminated waters even at very low concentrations. Their synthetic origin and complex aromatic structure makes them stable and difficult to be biodegraded [2]. Dyes can affect the photosynthetic activity and dissolved oxygen concentration in aquatic systems by preventing the transmission of light (reflection and absorption of sunlight), thus causing disturbance to the ecology of the receiving waters [3]. Dyes are also often highly toxic, carcinogenic, and mutagenic in nature, and can even bio-accumulate in the food chain [4]. The direct release of colored wastewaters into the aquatic ecosystems is, therefore, both environmentally unsafe and aesthetically unacceptable.

In view of the rising awareness of the importance of water quality preservation and improvement, the development of a clean and efficient water purification technology has been the focus of considerable research in the last few decades. Among the numerous treatment techniques that have been proposed, heterogeneous photocatalysis has emerged as one of the most powerful methods of water decontamination because of its potential to transform recalcitrant organic contaminants into mineral salts and relatively innocuous end products such as CO_2 and H_2O [5–7].

Heterogeneous photocatalysis involves the utilization of a semiconductor catalyst (such as TiO_2, ZnO, Fe_2O_3, CdS, GaP or ZnS), irradiated with light of an appropriate wavelength, to generate highly reactive transitory species (i.e., $\bullet OH$, $\bullet O_2^-$, $\bullet HO_2$) for mineralization of organic impurities [5,8]. This green technology offers a number of advantages such as ambient operating conditions, low operating costs, complete mineralization of organic pollutant without any secondary pollution, all of which have promoted its wide application in wastewater treatment [9]. Unfortunately, the insufficient quantum efficiency, narrow excitation wavelength, high recombination rate of the photoproduced electron–hole pairs, poor adsorption capacity, and deactivation of the semiconductor photocatalyst limit the practical application of this technique [10,11]. Even though a variety of approaches have been attempted to improve the photocatalytic behavior of semiconductors, including metal particle loading, co-catalysts, dye sensitization, metallic

* Corresponding author. Tel.: +65 65165135; fax: +65 67744202.
E-mail address: ceerbala@nus.edu.sg (R. Balasubramanian).

http://dx.doi.org/10.1016/j.apcatb.2014.05.035
0926-3373/

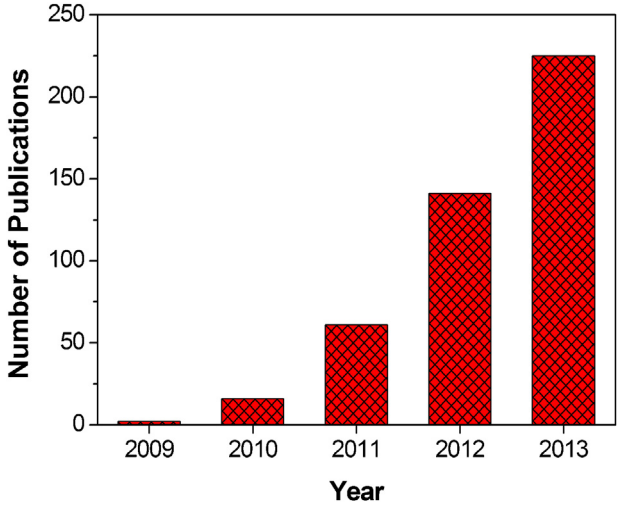

Fig. 1. Number of scientific articles published on GSN-mediated heterogeneous photocatalysis over the past five years (source: http://www.scopus.com; search terms: "graphene" and "photocatalysis").

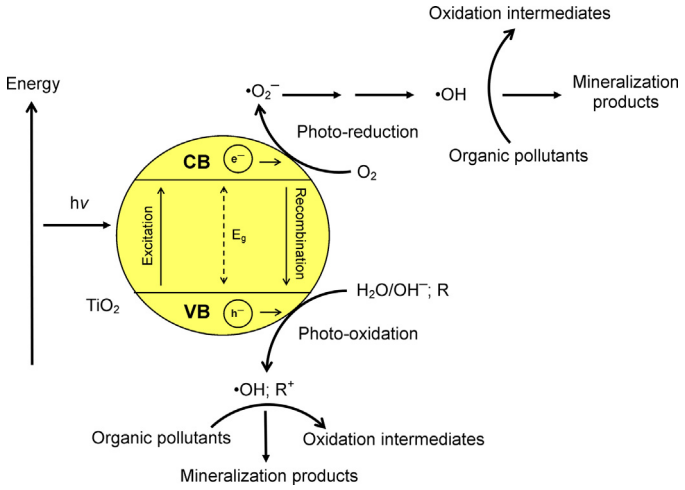

Fig. 2. Schematic of reactions occurring during heterogeneous photocatalysis over TiO_2. Adapted from [6].

doping and non-metallic doping, the development of an efficient and commercially viable photocatalyst still remains a significant challenge [12].

With rapid advancements in nanoscience and nanotechnology, much attention is currently directed toward harnessing the outstanding physicochemical properties of graphene – the newest member in the family of carbon allotropes – for designing next-generation photocatalyst systems with enhanced activity and performance. While other carbon nanomaterials such as fullerenes (C_{60}), carbon nanotubes (CNTs) and activated carbon are widely investigated for many years for photocatalytic applications with varying levels of success [12], graphene adds a new dimension to the ever progressing field of heterogeneous photocatalysis. Graphene is a single layer of sp^2 hybridized carbon atoms covalently packed into a continuous hexagonal lattice [13,14]. This one-atom-thick pseudo-infinite nano-crystal is characterized by a large theoretical specific surface area ($2630\,m^2\,g^{-1}$) [15], high electron mobility at room temperature ($200{,}000\,cm^2\,V^{-1}\,s^{-1}$) [16], exceptional thermal conductivity ($5000\,W\,m^{-1}\,K^{-1}$) [17], superior mechanical properties with Young's modulus of 1100 GPa [18], and excellent optical transmittance (97.7%) [19]. Such a combination of intriguing properties makes graphene an ideal electronic sink, or electron-transfer bridge and a 2D support matrix for photocatalyst carrier or promoter [10–12]. In view of these attractive attributes, there has been an increasing research interest in the recent times, seeking to couple graphene with photoactive semiconductors to develop graphene/semiconductor nanocomposites (GSNs) with high photocatalytic performance toward pollution control and abatement [10,11]. The conjugation of graphene with semiconductor solid particles results in photocatalysts with improved charge separation, reduced recombination of the photogenerated electron–hole pairs, increased specific surface area, and an adequate quantity and quality of adsorption sites [10]. In addition, recent developments have shown that the chemical relatives of graphene such as graphene oxide (GO) and reduced graphene oxide (rGO), because of their rich surface chemistry [20,21], also offer exciting opportunities for the development of novel photoactive nanocomposites for the transformation of environmental contaminants.

Since the first pioneering article in 2008 [22], scientific publications on the preparation and characterization of GSNs for photocatalytic applications appear to have risen almost exponentially (Fig. 1). GSN-mediated heterogeneous photocatalysis has been demonstrated to be an efficient tool for degrading a myriad of organic contaminants—the photodecomposition of synthetic dyes being rigorously investigated and reported. Despite some recent reviews on graphene-based nanocomposites for photocatalytic applications [10,11,23], the progress on photodecolorization of wastewaters contaminated with dyes has perhaps received less coverage than is warranted. The present review is thus an attempt to provide a comprehensive update of the key advancements in the development of GSNs for photodecolorization of textile effluents. The goal of the review is not just to integrate results from the studies reported in the literature, but identify current research directions and provide insights into the synthesis of GSNs and their photocatalytic performance for removal of selected dye pollutants. Moreover, the challenges posed on the commercial development of these novel composite photocatalysts and the scope for further enhancements of their photocatalytic activity have also been discussed for future research directions and opportunities.

2. Principle of heterogeneous photocatalysis

Heterogeneous photocatalysis is based on a complex sequence of reactions, the underlying principles of which are well established [24–26]. Briefly, when a semiconductor is illuminated with light energy, electrons (e^-) are excited from the valence band (VB) to the conduction band (CB). Electrons raised to the CB correspond to missing negative charges in the VB, called holes (h^+). Both the e^- and h^+ then migrate to the surface where they can initiate redox reactions with other chemical species adsorbed on the semiconductor. The photogenerated holes oxidize the hydroxyl groups or water molecules to produce •OH radicals while the photogenerated electrons reduce the dissolved oxygen to form superoxide radical anion ($•O_2^-$) [6,27], which then reacts with H^+ to form $•HO_2$, followed by rapid decomposition to •OH [28]. The •OH radical, being a very strong oxidizing agent (standard redox potential +2.8 V vs. normal hydrogen electrode) oxidizes the surface adsorbed organic pollutant into readily biodegradable compounds [29]. The basic photophysical and photochemical processes involved during heterogeneous photocatalysis are illustrated in Fig. 2 and are often represented by the following chain reactions [6,29,30]:

$$\text{Photoexcitation}: \quad SC + h\nu \rightarrow SC\ (e^- + h^+) \tag{1}$$

$$\text{Ionization of water}: \quad SC\ (h^+) + H_2O \rightarrow •OH + H^+ \tag{2}$$

$$\text{Oxygen ionosorption}: \quad SC\ (e^-) + O_2 \rightarrow •O_2^- \tag{3}$$

$$\text{Protonation of superoxide: } \bullet O_2^- + H^+ \rightarrow \bullet HO_2 \quad (4)$$

$$\bullet HO_2 + H^+ + SC(e^-) \rightarrow H_2O_2 \quad (5)$$

$$H_2O_2 + (SC)e^- \rightarrow \bullet OH + OH^- \quad (6)$$

$$\text{Decomposition of pollutant: Pollutant} + h^+ \rightarrow \text{Oxidation products} \quad (7)$$

$$\text{Pollutant} + e^- \rightarrow \text{Reduction products} \quad (8)$$

$$\text{Pollutant} + \bullet OH \rightarrow \text{Degradation products} \quad (9)$$

where SC = semiconductor.

The key to a successful photocatalytic reaction is the absorption of photons to create e^-/h^+ pairs. The energy of the incident light must be greater than the semiconductor band gap energy if an electron is to be photoexcited from the VB to the CB [24]. Many of the commonly used semiconductors have wide band gaps and can thus only be excited under irradiation of UV light. Because of the staggering amount of solar energy that reaches the Earth's surface in the form of visible light (>50% of the total energy from the sun) [31], it would be more rational to develop photocatalysts capable of utilizing this perpetual energy source.

Another important factor that must be considered is the e^-/h^+ trapping or recombination rates. Since the recombination timescale of e^- and h^+ is of the order of nanoseconds (as determined by time resolved spectroscopic studies) [12,29], it is extremely important to provide adequate scavengers for these charge carriers in the aqueous system to have favorable photocatalyzed reaction [29]. In addition, heterogenous photocatalysis also demands for the adsorption of the pollutant on the photocatalyst surface as a prerequisite step. Therefore, by concentrating the target pollutant around the semiconductor surface, it is possible to improve the efficiency of a photocatalytic reaction because the pollutant can then react readily with the short-lived •OH radicals, and also serve as scavengers for e^- and h^+.

Graphene, as a new material, has the potential to contribute to all of these fundamental methods of enhancing the photocatalytic activity and performance of semiconductors. Graphene is a zero band gap semimetal with massless Dirac fermions being the charge carriers [32,33]. It can thus absorb light over a broad range of wavelengths, facilitating visible light catalysis. In addition, the excellent charge trapping ability of graphene nanosheets can be utilized to retard the e^-/h^+ recombination [13]. Moreover, owing to its infinitely large surface-to-volume ratio, graphene has a propensity to adsorb a wide range of synthetic organic compounds as well as inorganic substances [34]. Hence, the development of GSNs (having more versatile and tailor-made properties) is an innovative approach to improve the application of semiconductor nanomaterials in heterogeneous photocatalysis.

3. Synthesis of GSNs

Till date, a wide range of semiconductor materials have been supported on graphene-based templates. These mainly include metal oxides (e.g., TiO_2 [35–40], ZnO [41–46], Cu_2O [47], Fe_2O_3 [48], Mn_2O_3 [49], WO_3 [50]), metal sulfides (e.g., CdS [51,52], In_2S_3 [53], Sb_2S_3 [54]), metallates (e.g., $BiVO_4$ [55], $CoFe_2O_4$ [56]; Bi_2WO_6 [57], Bi_2MoO_6 [58]), and other semiconducting nanoparticles (e.g., CdSe [59], $Zn(CH_3COO)_2$ [60]). Interestingly, a variety of techniques have also been developed for preparing such composite photocatalysts. Many of these procedures are similar to those used for other nanocomposite systems although some of them have been put forward uniquely for the fabrication of GSNs. Nevertheless, they can all be divided into two basic categories: in situ crystallization and ex situ hybridization.

3.1. In situ crystallization

In situ crystallization is the most common strategy for the synthesis of GSNs. It involves the formation of nanocrystallites in the presence of graphene precursors (e.g., GO), followed by their direct growth into nanomaterials such as nanoparticles, nanowires, nanorods, or nanofilms on the surface of GO nanosheets, and subsequent reduction of GO to generate graphene-based nanocomposite [61]. Such an approach allows homogeneous distribution of nanocrystals on the 2D nanosheets due to nucleation of nanoparticles in situ. The oxygen functional groups on GO can be utilized as nucleating sites to control the size, morphology and crystallinity of the in situ grown nanoparticles. Additionally, the direct contact of semiconductor nanoparticles with graphene sheets enhances the electron transport rate between them [62].

3.1.1. Solution mixing

This simple and straightforward technique involves the mixing of colloidal suspension of GO platelets or other graphene-based materials with the desired semiconductor precursors under vigorous stirring or ultrasonic agitation. During the blending, the precursors are readily transformed into products, which then uniformly distribute themselves over the surface of the individual sheets and interconnect each sheet when the solvent is evaporated, to form the composite [20]. Graphene-based nanocomposites can be finally obtained by the reduction of GO in the composite using reducing agents like amines, sodium borohydrate and ascorbic acid. Guo et al. [63] synthesized graphene/TiO_2 composites by ultrasonically mixing titanium tetrachloride ($TiCl_4$) and GO in ethanol–water system, followed by a hydrazine treatment to reduce GO into graphene. Similarly, GO dispersion have been mixed together with silver nitrate ($AgNO_3$) and cetyltrimethylammonium bromide (CTAB) by vigorous stirring, followed by reduction of GO to yield Ag/AgBr/rGO nanocomposites [64]. It is important to note here that long time exposure to high power ultrasonication can induce defects in graphene sheets which are detrimental to the composite properties. Chemical functionalization can improve the solubility and interaction of graphene materials with the nanoparticles, and may also help in obtaining a higher loading rate [65].

3.1.2. Hydrothermal/solvothermal process

Hydrothermal process is the most widely used method for synthesis and fabrication of GSNs. It involves the utilization of single, or heterogeneous phase reactions in aqueous media at elevated temperature and pressure to crystallize metal-based nanostructures directly from solution onto GO sheets and at the same time reduce GO to graphene/rGO depending on the reaction conditions [66]. A more general term 'solvothermal' refers to a similar reaction in which a different solvent (organic or inorganic) is used [67]. Usually, hydro(solvo)thermal reactions are carried out in an autoclave (a steel pressure vessel) at temperatures above the boiling point of the solvent to self-generate saturated vapor pressure. For instance, $BiVO_4$–graphene nanocomposites were obtained when bismuth nitrate ($Bi(NO_3)_3{\cdot}5H_2O$) and ammonium metavanadate (NH_4VO_3) were mixed with GO sheets suspended in aqueous medium and heated in an autoclave at 180 °C for 6 h [55]. Similarly, Pant et al. [68] fabricated flower-shaped ZnO doped rGO composite material by simultaneous crystal growth (of ZnO) and reduction (of GO) using hydrothermal process as illustrated in Fig. 3. Ternary composites such as magnetic graphene–Fe_2O_3/ZnO nanocomposites have also been prepared by hydrothermal method, using GO and zinc hydroxide ($Zn(OH)_2$) as the precursors for graphene and ZnO, respectively, and commercially available Fe_2O_3 as a magnetic

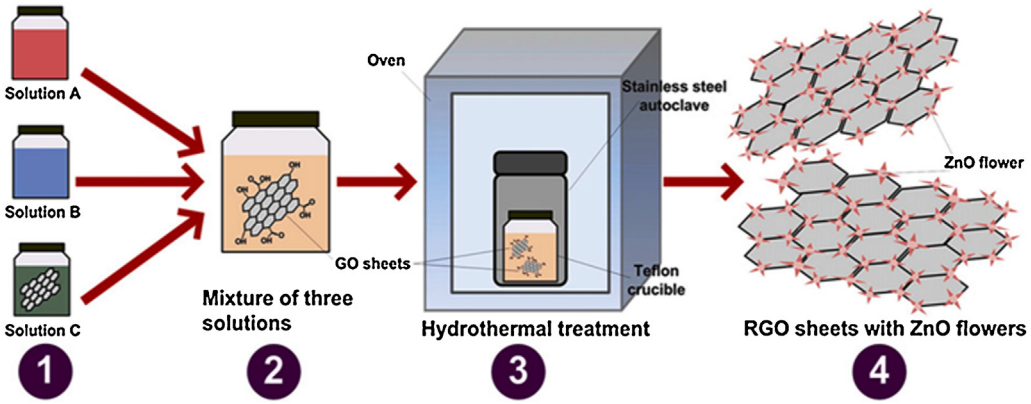

Fig. 3. Schematic of the growth of ZnO flowers on the surface of rGO sheets by hydrothermal treatment at 140 °C for 2 h (Solution A: bis(hexamethylene)triamine; Solution B: zinc nitrate hexahydrate; Solution C: aqueous colloidal suspension of GO). Reprinted from [69], Copyright 2012, with permission from Elsevier.

material [69]. Wang et al. [51] synthesized rGO/CdS nanocomposites by a solvothermal method, wherein a mixture of GO and cadmium acetate ($Cd(CH_3COO)_2$) in dimethylsulfoxide (DMSO) was heated in an autoclave at 180 °C for 12 h. GO served as the supporting material and $Cd(CH_3COO)_2$ as the CdS precursor, while DMSO acted as both the solvent and the sulfur source. Tao et al. [54] fabricated novel graphene–Sb_2S_3 composites via a facile solvothermal method with GO, antimony trichloride ($SbCl_3$) and thiourea ($CS(NH_2)_2$) as the reactants.

Hydrothermal/solvothermal techniques have been increasingly adopted for synthesizing GSNs since they offer several advantages compared with other processes: (a) high reactivity, (b) low energy requirement, (c) mild reaction conditions, (d) relatively non-polluting set-up and (e) simple control of the solvent [70]. The reaction pathway is, however, very sensitive to the experimental conditions, such as pH, temperature and hydro(solvo)thermal treatment time, but can still give a high yield of nanocomposites at low cost and in a relatively simpler manner under optimized conditions [70].

3.1.3. Sol–gel method

The sol–gel process is a useful and versatile wet chemical approach to the engineering and preparation of GSNs. It is based on the phase transition of a system from a colloidal liquid called "sol" into a solid gel through a series of hydrolysis and polycondensation reactions [71,72]. The starting materials used in the preparation of the sol are usually metal alkoxides, metal chlorides or organometallic compounds. Li et al. [73] adopted a sol–gel route to fabricate graphene–TiO_2/silica nanocomposites. They added tetraethyl orthosilicate ($Si(OC_2H_5)_4$), titanium tetrachloride ($TiCl_4$), and titanium tetraisopropoxide ($Ti\{OCH(CH_3)_2\}_4$) into an ethanol dispersion of graphene sheets in the presence of non-ionic surfactant P123. After stirring the resulting mixture for 24 h at room temperature, a semi-transparent sol was obtained which was then subjected to hydrothermal treatment at 150 °C for 48 h. Li et al. [74] also prepared graphene–tourmaline–TiO_2 composites by using a direct sol–gel co-condensation combined with solvothermal treatment technique.

The key benefit of the sol–gel approach is that the surface —OH groups of the GO/rGO sheets act as nucleation sites for hydrolysis. As a consequence, the resulting metal oxide nanostructures are chemically bonded to the GO/rGO surfaces [75]. Additional and widely recognized advantages of the sol–gel method include low process temperature, ability to control the composition on molecular scale, and high purity and homogeneity of the final product [71,72]. However, one of the major drawbacks of the sol–gel approach is that the product typically consists of an amorphous phase rather than defined crystals and, thus, requires crystallization and post annealing steps [61].

3.1.4. Combustion synthesis

Combustion synthesis is another important technique for the in situ preparation of GSNs. It is characterized by high-temperatures, fast heating rates, short reaction times, limited energy consumption and complete conversion of the reactants to products [76,77]. In addition, the process relies on simple and low cost facilities and equipment, and yields high purity products with fine particles (since high temperatures expel the volatile impurities) [77,78]. These features make combustion synthesis an attractive alternative to the above mentioned preparation strategies for GSNs.

In this method, stoichiometric amounts of the graphene material and a semiconductor precursor (e.g., metal nitrate) are pre-mixed together, to which an organic fuel (e.g., urea, glycine, hydrazides) is added. The resulting gel-like mixture is then dehydrated and subsequently ignited by an external energy source [79]. Upon ignition, the exothermicity of the combustion process provides the energy requirement for the synthesis reaction to transpire. The hot combustion waves self-propagate at very high velocities through the heterogeneous mixture of reactants, yielding the desired product [76,79]. Combustion synthesis has been successfully implemented to synthesize a variety of GSNs. For example, Gao et al. [80] reported the in situ synthesis of GO–TiO_2 nanocomposites through combustion synthesis reaction of titanyl nitrate ($TiO(NO_3)_2$) and urea.

3.1.5. Microwave-assisted deposition

In recent years, microwave irradiation has emerged as an important tool for the synthesis of both organic and inorganic materials with controlled size and shape [81,82]. Its rapid and homogeneous heating properties offers a fast and convenient approach to prepare graphene/metal compound hybrids by the simultaneous reduction of GO and metal salts. Hu et al. [83] reported a microwave-assisted synthesis of graphene/ZnS nanocomposites in aqueous medium. In that experiment, GO and zinc acetate dihydrate ($Zn(CH_3COO)_2{\cdot}2H_2O$) were reduced simultaneously with thioacetamide during the microwave irradiation process. Microwave-assisted methods have also been used to prepare BiOBr/graphene [84] and rGO/ZnO [43,85,86] composites. Compared to the other in situ approaches, microwave-assisted synthesis allows selective activation of the target precursor to initiate nucleation thereby generating smaller and more uniform particles. Importantly, it is also possible to program and to control the different synthesis steps.

3.1.6. Electrochemical deposition

Electrochemical deposition is another simple, fast and clean method of fabricating GSNs. In this process, inorganic nanostructures can be directly deposited on the surface of graphene-based substrates by simple electrolysis of an aqueous solution containing the desired metal ion or its complex, without the requirement for post-synthetic transfer of the composite materials [75]. For example, Wei et al. [46] fabricated graphene–ZnO hybrids through in situ electrodeposition of ZnO on GO-coated ITO (indium tin oxide) glass electrodes, using aqueous solution of zinc nitrate ($Zn(NO_3)_2$) as the electrolyte. The deposition was carried out using potential of −1.1 V vs. SCE (saturated calomel electrode) at 50 °C for 1000 s. GO was electrochemically reduced to graphene and the change of the electrochemical interface between the electrode and the electrolyte provided a favorable condition for the simultaneous growth of ZnO. The following reactions were believed to occur during the formation of G-ZnO hybrid by electrochemical deposition:

$$GO + NO_3^- + H_2O + 2e^- \rightarrow NO_2^- + G + 2OH^- \quad (10)$$

$$Zn^{2+} + 2OH^- \rightarrow Zn(OH)_2 \xrightarrow{\Delta} ZnO + H_2O \quad (11)$$

The electrochemical synthesis approach offers the advantages of low-temperature conditions, high-throughput mass production and low-cost, and has thus attracted much attention as a viable route to afford GSNs.

3.1.7. Photo-assisted reduction

Recently, photo-assisted methods have also attracted considerable attention in the synthesis of GSNs. Photochemical reduction by irradiating a graphene precursor in the presence of metal salts provides a convenient way to produce GSNs. For example, Barras et al. [87] reported the photo-assisted synthesis of Au@Mo–GO composites with the UV irradiation of an aqueous mixture of GO, $Na_2[Mo_6Br_8(N_3)_6]$, and $HAuCl_4{\cdot}3H_2O$ in the presence of isopropanol. Besides, photo-assisted reduction in the fabrication of WO_3@graphene [50] and graphene–Au [88] nanocomposites have also been reported. The photoinduced synthesis approach has many advantages since it combines the characteristic features of light activation i.e., ease and versatility of the process, high spatial resolution and reaction controllability (intensity and wavelength), with the simplicity of the colloidal approach. It can also provide a uniform reducing environment in solution and no additional reagents are required [61].

3.2. Ex situ hybridization

Ex situ hybridization involves the mixing of pre-synthesized or commercially available nanocrystals with colloidal suspension of graphene-based templates [75], wherein the inorganic nanoparticles attach to the 2D nanosheets through binding with oxygen containing surface functional moieties of GO/rGO. For example, Nguyen-Phan et al. [89] prepared TiO_2/GO composites by mixing commercial TiO_2 (P25, Degussa) with GO in deionized water. Gao et al. [90] fabricated GO–CdS nanocomposites by mixing CdS nanoparticles, pre-synthesized through a hot-injection method, with aqueous suspension of GO sheets. GO in the composite photocatalyst may be further reduced by chemical and/or thermal methods to yield graphene-based composite. Prior to mixing, surface modification of the nanocrystals and/or the nanosheets can be carried out to increase the loading rate of the inorganic nanoparticles on the graphene-based nanosheets. This self-assembly based method is excellent at overcoming any incompatibilities between nanomaterials syntheses and the formation of nanocomposites, and also allows co-assembly of nanoparticles with distinctively different sizes, compositions, shapes, and properties on GO/rGO sheets [61]. However, unlike the in situ techniques, ex situ hybridization suffers from low density and non-uniform coverage of the nanostructures on the surface of GO/rGO [20,75].

4. Photocatalytic degradation of synthetic dyestuffs by GSNs

4.1. Methylene blue

Methylene blue (MB) is a water-soluble thiazine dye, commonly used for dyeing of silk, leather, plastics, paper, cotton mordanted with tannin, and also in the manufacture of paints and printing inks [91]. In the dairy industry, MB is used to determine the microbial load in milk [92]. On inhalation, MB can give rise to short periods of rapid or difficult breathing while ingestion through the mouth produces a burning sensation and may cause hypertension, precordial pain, dizziness, headache, fever, fecal discoloration, profuse sweating, mental confusion, methemoglobinemia, and hemolytic anemia [93,94]. To prevent its harmful impacts on receiving waters, the photocatalytic degradation of MB is of great importance in water treatment and has been widely carried out using many different kinds of GSNs, especially TiO_2/graphene as shown in Table 1.

Zhou et al. [36] prepared graphene/TiO_2 (G/TiO_2) composites through a one-pot solvothermal reaction by using GO and tetrabutyl titanate ($C_{16}H_{36}O_4Ti$) as starting materials. TiO_2 particles with anatase phase and a narrow size distribution were uniformly dispersed on the surface of graphene sheets. The as-synthesized nanocomposite exhibited significantly enhanced photodegradation of MB over pure TiO_2 upon irradiation with simulated sunlight. Fluorescence quenching studies confirmed that graphene acted as an electron-acceptor material to effectively hinder the e^-/h^+ pair recombination of TiO_2, resulting in enhanced photocatalytic activity. Lee et al. [96] decorated graphene sheets with TiO_2 nanorods by a simple non-hydrolytic sol–gel approach to develop novel photocatalyst systems with improved activity and performance. Compared to pristine TiO_2 nanorods as well as commercial TiO_2 (Degussa P25), the G/TiO_2 nanorod composite showed unprecedented photodecomposition efficiency (∼100%) for MB under both UV and visible light. In another study, Nguyen-Phan et al. [89] demonstrated the excellent photocatalytic performance of GO/TiO_2 composite materials under both UV and visible radiation for degradation of MB. The authors explained that irrespective of the light sources, the synergistic effect of GO's large surface area and oxygen-containing surface functional moieties improved the adsorption of dye molecules and the separation efficiency of e^- and h^+, thereby enhancing the photocatalytic performance. rGO/TiO_2 composites have also been found to be at least 6 times more effective for photodegradation of MB than by Degussa P25, whether it was under UV or visible light illumination [39]. Similar reports confirming the superior photocatalytic activity of graphene-based TiO_2 composites toward MB under both UV and visible light are widely available in the literature [35,38,40,95,97,98,100,106,111,113,122].

In addition, graphene-based ZnO composites have also been widely studied for photocatalytic decomposition of MB. Xu et al. [41] synthesized ZnO/graphene (ZnO/G) nanocomposites for photocatalytic degradation of MB under UV irradiation. As shown in Fig. 4, the photoactive nanocomposite exhibited an outstanding performance in decomposing MB and its activity was improved by a factor of about 4 and 5 relative to the activity of mechanical mixture of ZnO and graphene and pure ZnO, respectively. These results suggest that intimate contact between semiconductor and graphene material is crucial for the formation of electronic interaction and inter-electron transfer at the interface. In another study, Fan et al. [42] prepared a series of ZnO/G composites with different ZnO

Table 1
Photocatalytic degradation of MB by GSNs in aqueous solutions.

Photoactive nanocomposite	Initial dye conc.	Catalyst dose ($g L^{-1}$)	Light source	Irradiation time (min)	Degradation (%)	Reference
Graphene/TiO_2	1.0×10^{-5} M	1	Simulated sunlight	480	>75	[36]
TiO_2/graphene	1.0×10^{-5} M	–	Visible	180	~55	[35]
TiO_2/graphene	2.0×10^{-5} M	0.1	Visible	60	71	[95]
TiO_2/graphene	2.0×10^{-5} M	0.1	UV	12	98	[95]
Graphene–TiO_2 nanorod	3.0×10^{-5} M	0.75	Visible	180	~100	[96]
Graphene–TiO_2 nanorod	3.0×10^{-5} M	0.75	UV	20	~100	[96]
Graphene–TiO_2	20 mg L^{-1}	1	UV	60	94	[37]
Graphene@TiO_2	10 mg L^{-1}	0.5	UV	<100	88	[38]
Graphene@TiO_2	10 mg L^{-1}	0.5	Visible	200	52	[38]
Graphene/TiO_2	2.0×10^{-5} M	0.3	UV	150	>90	[97]
Graphene/TiO_2	2.0×10^{-5} M	0.3	Visible	150	>60	[97]
Graphene–TiO_2	10 mg L^{-1}	0.5	UV	110	100	[40]
Graphene–TiO_2	10 mg L^{-1}	0.5	Visible	150	95	[40]
Graphene–TiO_2	1.56×10^{-3} M	0.75	UV	30	>90	[98]
TiO_2–Graphene/carbon composite nanofibers	–	–	Visible	30	100	[99]
P25–graphene	10 mg L^{-1}	0.75	Visible	55	100	[100]
P25–graphene	10 mg L^{-1}	0.75	UV	55	96	[100]
P25–graphene	10 mg L^{-1}	0.4	UV	200	>90	[101]
Graphene–Bi_2MoO_6	1.0×10^{-5} M	0.5	Visible	120	80	[58]
$CoFe_2O_4$–graphene	20 mg L^{-1}	0.25	Visible	240	100	[56]
Graphene–Cu_2O	10 mg L^{-1}	0.4	Visible	120	90	[47]
La/TiO_2–graphene	10 mg L^{-1}	1	Visible	60	>80	[102]
Graphene–Mn_2O_3	1.2×10^{-5} M	0.5	UV	160	84	[49]
γ-Fe_2O_3/SiO_2/graphene/TiO_2	20 mg L^{-1}	2	UV	60	100	[103]
γ-Fe_2O_3/SiO_2/graphene/TiO_2	20 mg L^{-1}	2	Visible	60	90	[103]
Graphene/ZnS	15 mg L^{-1}	0.2	UV	32	100	[83]
ZnO/graphene	1×10^{-5} M	0.5	UV	40	>90	[41]
ZnO/graphene	10 mg L^{-1}	0.5	UV	56	72.1	[42]
ZnO/graphene	20 mg L^{-1}	1	Visible	90	99.5	[45]
Graphene–ZnO	–	–	UV	180	100	[46]
Graphene–ZnO	–	–	Visible	180	100	[47]
Graphene–Fe_2O_3/ZnO	10 mg L^{-1}	0.2	Sunlight	90	99.5	[69]
$ZnFe_2O_4$/ZnO/graphene	10 mg L^{-1}	0.14	Simulated sunlight	100	~100	[104]
$Cd_xZn_{1-x}S$/graphene	20 mg L^{-1}	0.5	Visible	50	>90	[105]
$BiVO_4$–graphene	20 mg L^{-1}	0.5	Visible	300	99	[55]
TiO_2/GO	2.5×10^{-5} M	0.2	UV	60	100	[89]
TiO_2/GO	2.5×10^{-5} M	0.2	Visible	60	95	[89]
TiO_2–GO	10 mg L^{-1}	0.5	Visible	180	>80	[39]
TiO_2–GO	10 mg L^{-1}	0.5	UV	12	100	[39]
TiO_2–GO	20 mg L^{-1}	1.5	Visible	420	~90	[106]
GO–$BiPO_4$	20 mg L^{-1}	0.5	Simulated sunlight	240	100	[107]
ZnO–Bi_2O_3/GO	10 mg L^{-1}	0.5	Visible	120	99.62	[108]
ZnO/GO	5.0×10^{-5} M	0.8	Visible	60	98.1	[45]
GO/Ag_3PO_4	25 mg L^{-1}	0.5	Visible	60	99.8	[109]
GO–Ag_3PO_4	7.5 mg L^{-1}	0.3	Visible	24	100	[110]
rGO/TiO_2	10 mg L^{-1}	0.5	Visible	180	100	[39]
rGO/TiO_2	10 mg L^{-1}	0.5	UV	8	100	[39]
rGO/TiO_2	10 mg L^{-1}	0.5	Visible	120	94.1	[111]
rGO/TiO_2	10 mg L^{-1}	0.5	UV	110	100	[111]
rGO/TiO_2 nanorod	20 mg L^{-1}	0.2	UV	45	>80	[112]
N-P90/N–rGO	2.0×10^{-5} M	0.5	Visible	160	~80	[113]
ZnO–rGO	5 mg L^{-1}	1.5	UV	260	88	[85]
rGO/ZnO	10 mg L^{-1}	0.125	Visible	40	>95	[86]
ZnO–rGO	5.0×10^{-5} M	0.4	UV	130	>80	[114]
ZnO/rGO	10 mg L^{-1}	0.5	UV	180	>90	[68]
rGO/ZnO	1.0×10^{-5} M	5	UV	40	100	[60]
rGO/ZnO	10 mg L^{-1}	0.5	UV	60	100	[111]
rGO/ZnO	10 mg L^{-1}	0.25	Simulated sunlight	200	90	[115]
rGO/ZnO/CTAB	10 mg L^{-1}	0.25	Simulated sunlight	200	150	[115]
rGO/Ta_2O_5	10 mg L^{-1}	0.5	UV	120	72.1	[111]
rGO–$CoFe_2O_4$	10 mg L^{-1}	0.16	Visible	180	>85%	[116]
rGO–CdS	100 mg L^{-1}	0.16	Visible	150	94	[51]
CuS/rGO	4 mg L^{-1}	0.1	Visible	120	81	[117]
ZnS–rGO	6.25×10^{-5} M	1	Visible	60	79	[118]
Ag_3PO_4/rGO	10 mg L^{-1}	0.28	Visible	90	72	[119]
rGO–Bi_2WO_6	15 mg L^{-1}	0.5	Visible	90	93.5	[57]
Bi_2O_3–rGO	5 mg L^{-1}	2	Visible	240	96	[120]
rGO/$Zn_{0.8}Cd_{0.2}S$	1.0×10^{-5} M	0.5	Visible	120	96	[121]

to graphene mass ratio by a simple and non-toxic hydrothermal method and tested their efficacy in photodecomposing MB. Under UV light irradiation, the ZnO/G composite with mass ratio 50:1 showed the highest photocatalytic efficiency. Its rate of degradation was remarkably higher than that of commercial P25 and bare ZnO nanoparticles. Furthermore, the presence of graphene inhibited the photocorrosion of ZnO to a large extent. Similar results have also been obtained by Fu et al. [123], Ahmad et al. [45] and Wei et al.

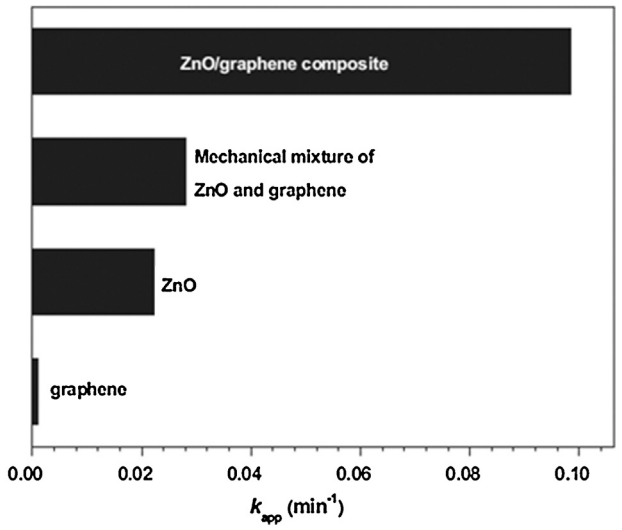

Fig. 4. The apparent rate constant of MB photodegradation on graphene, ZnO, mechanical mixture of ZnO and graphene, and the ZnO/graphene composite. Reprinted from [41], Copyright 2011, with permission from Elsevier.

[46] for photocatalytic breakdown of MB by ZnO/G. Li et al. [44] fabricated ZnO/GO nanocomposite via a facile chemical deposition route and used it for the photodegradation of MB under visible light. The composite demonstrated an outstanding photocatalytic efficiency of 98.1% which was ascribed to the efficient photosensitized electron injection and repressed electron recombination due to the electron-transfer process with GO as electron collector and transporter. Lv et al. [85] found that incorporation of rGO can also enhance the photocatalytic performance and photostability of ZnO in degradation of MB. The ZnO/rGO composite attained a maximum degradation efficiency of 88% at pH 7 under UV light irradiation for 260 min as compared with pure ZnO (68%). ZnO/rGO composites have also been found to be effective for photodecolorizing MB solutions by various other researchers [60,68,86,111,114,115].

Apart from these composites, a variety of other metal oxide semiconductors have also been studied in the preparation of graphene-based photocatalysts for degradation of MB. For example, Gao et al. [47] developed graphene–Cu_2O composites by a simple and efficient one step method and evaluated its photocatalytic activity for decolorizing aqueous solutions of MB. As much as 90% dye removal was achieved upon visible light irradiation for 120 min. Chandra et al. [49] synthesized graphene–Mn_2O_3 composites using a sonochemical method. The reactivity of the composite under UV irradiation was considerably higher than that of bare Mn_2O_3 nanoparticles for MB. Sun et al. [111] studied the photocatalytic performance of rGO/Ta_2O_5 composites for degrading MB under both UV and visible irradiations. The composite was not effective to degrade MB under visible light whereas about 72% of the dye was decomposed after 120 min of UV irradiation.

Zhou et al. [58] fabricated graphene–γBi_2MoO_6 (G–γBi_2MoO_6) composites by a facile one-step hydrothermal method and examined its photocatalytic performance for degradation of MB under visible light. Photodecomposition of MB by G–γBi_2MoO_6 followed pseudo-first-order kinetics with a reaction rate constant almost four times faster than that of pure Bi_2MoO_6 ($k_{G-\gamma Bi_2MoO_6} = 0.0136\,min^{-1}$; $k_{\gamma Bi_2MoO_6} = 0.0037\ min^{-1}$). Xu et al. [57] compared the photocatalytic activities of pure Bi_2WO_6 and rGO–Bi_2WO_6 composite samples for degradation of MB under visible light irradiation. The results suggested that introduction of rGO distinctly enhanced the photoactivity of Bi_2WO_6. Similar results have also been reported by Fu et al. [55] and Lv et al. [107] who studied the photocatalytic removal of MB by $BiVO_4$–graphene and GO–$BiPO_4$ composites, respectively.

In order to remove catalysts effectively and readily, magnetically separable graphene-based composite photocatalyst have been developed by anchoring $CoFe_2O_4$ nanoparticles onto graphene sheets [56]. Photocatalytic activity tests showed that the $CoFe_2O_4$–graphene composites induced complete photodecomposition of MB under visible light irradiation. In addition, the composites could be easily separated from the bulk solution by applying an external magnetic field. A similar trend was observed for photocatalytic removal of MB by rGO–MFe_2O_4 (M = Mn, Zn, Co and Ni) hybrids. [116].

Different metal sulfides have also been combined with graphene materials to develop novel photocatalyst systems with enhanced activity for photodecomposition of MB. For instance, Hu et al. [83] explored graphene/ZnS composites for photodegradation of MB. Complete decomposition of the dye was obtained after just 32 min of UV irradiation. Wang et al. [51] fabricated rGO/CdS nanocomposites for photocatalytic removal of MB from aqueous environment. The composite exhibited enhanced photoactivity under visible light irradiation than pure CdS nanoparticles. Xiong et al. [124] also found that photocatalytic degradation of MB by CdS was significantly improved following its combination with rGO. Zhang et al. [117] developed CuS/rGO nanocomposites with the use of L-cysteine, an amino acid, as a reducing agent, sulfur donor, and linker to anchor CuS nanoparticles onto the surface of rGO sheets. Upon visible light illumination, the CuS/rGO nanocomposites showed pronounced photocurrent response and improved photocatalytic activity in the degradation of MB compared to pure CuS. In a recent study by Wang et al. [105], $Cd_xZn_{1-x}S$ nanoparticles with uniform size and small diameter were immobilized onto graphene sheets by a one-step solvothermal route. The as-prepared composites of $Cd_xZn_{1-x}S$/graphene showed better photocatalytic activity than pure $Cd_xZn_{1-x}S$ nanoparticles for MB because of efficient charge separation of the photogenerated e^-/h^+ pairs due to the presence of graphene. rGO/$Zn_{0.8}Cd_{0.2}S$ hybrid nanomaterials, synthesized via a solvothermal method, have also been found to exhibit much higher photocatalytic activity than pure $Zn_{0.8}Cd_{0.2}S$ nanoparticles for the degradation of MB [121].

Recently, Ao and colleagues have demonstrated the feasibility of applying GO/Ag_3PO_4 for photodegradation of MB under visible light irradiation [109]. Photocatalytic activity measurements showed that the dye solution was almost completely decolored by the composite within 1 h of visible light illumination. The excellent photocatalytic activity of GO/Ag_3PO_4 was attributed to its high adsorption activity and high migration efficiency of photoinduced electrons at the interface of Ag_3PO_4 and GO. The effect of GO amount on the photocatalytic efficiency of the as-prepared composite photocatalysts was also investigated. Results suggested that GO content of about 10% was sufficient for optimum photocatalytic activity. Bai et al. [110] also investigated the photocatalytic degradation of MB using GO/Ag_3PO_4 nanocomposites and observed that complete dye degradation could be achieved within about 24 min exposure to visible light. More recently, Ag_3PO_4/rGO composites have also been found to be effective for photocatalytic decomposition of MB under visible light irradiation [119].

Beyond binary GSNs, considerable research efforts have been directed recently toward the development of graphene-based ternary composite systems for further enhancements in photocatalytic activity and improvement of the visible light absorption of the solar spectrum. Kim et al. [99] synthesized TiO_2–graphene/carbon composite nanofibers (TiO_2–CCNF) by depositing TiO_2 nanoparticles onto electrospun graphene/carbon composite nanofibers (CCNFs) using the sol–gel method. The photodecomposition efficiency of the ternary composite for MB under visible light irradiation was evaluated and compared with that of carbon nanofibers

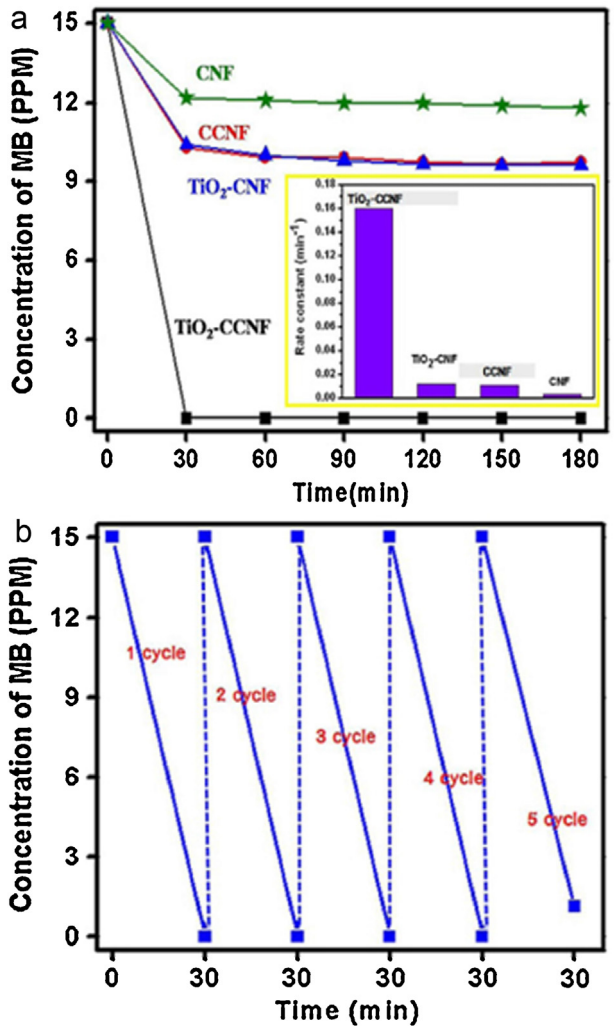

Fig. 5. (a) Photocatalytic performance of TiO_2–CCNF, TiO_2–CNF, CCNF and CNF for degradation of MB under visible light irradiation (inset: average reaction rate constants (min^{-1}) for photodegradation of MB). (b) Photocatalytic activity of TiO_2–CCNF hybrids for degradation of MB over five degradation cycles. Reprinted from [99], Copyright 2012, with permission from Elsevier.

(CNFs), CCNF and TiO_2–CNF. Experimental results showed that TiO_2–CCNF had a higher efficiency for decomposition of MB than CNFs, CCNF and TiO_2/CNF (Fig. 5a). The photocatalytic breakdown of MB followed pseudo-first-order kinetics, and the rate constant for TiO_2–CCNF ($k = 0.16\ min^{-1}$) was found to be much larger than those for TiO_2–CNF ($k = 0.012\ min^{-1}$), CCNF ($k = 0.011\ min^{-1}$), and CNFs ($k = 0.003\ min^{-1}$). Additionally, the stability of the TiO_2–CCNF material was also examined. As shown in Fig. 5b, the photocatalytic degradation of MB by TiO_2–CCNF was consistently effective over five degradation cycles.

Khalid et al. [102] prepared La/TiO_2–graphene composites by a two-step hydrothermal method. The composite photocatalyst was found to be remarkably more active than pure TiO_2 under visible light irradiation for MB degradation. The enhanced photoactivity was ascribed to extended light absorption, efficient charge separation, improved adsorption uptake and possibility of more π–π interaction between the composite and dye molecules. Khalid and co-workers [125] also reported that graphene–Ag/ZnO composites, synthesized via a simple single step solvothermal method, exhibit excellent photocatalytic activity in degrading MB. Complete degradation of MB was achieved after 90 min of visible light irradiation. Sun et al. [104] successfully developed $ZnFe_2O_4$/ZnO/graphene ($ZnFe_2O_4$/ZnO/G) ternary composites by immobilizing $ZnFe_2O_4$/ZnO binary nanocomposites onto graphene sheets using an ultrasound aided solution mixing method. $ZnFe_2O_4$/ZnO/G showed a high photocatalytic activity for degradation of MB in sunlight. The photocatalysis of MB by $ZnFe_2O_4$/ZnO/G could be described in terms of Langmuir–Hinshelwood model. Furthermore, the novel photocatalyst could be conveniently separated and recycled by an external magnetic field due to its high intrinsic magnetism. Vijay Kumar et al. [69] also synthesized magnetically separable visible light driven graphene–Fe_2O_3/ZnO composites that were capable of degrading MB efficiently even after five cycles of photocatalysis.

ZnO–Bi_2O_3/GO is another ternary GSN that has been recently studied for the photodegradation of MB [108]. It was found that the photodegradation of MB in the presence of ZnO–Bi_2O_3/GO reached 99.62% after irradiation with visible light for 2 h. The introduction of GO enhanced the stability of ZnO–Bi_2O_3 and reduced the recombination of charge carriers. Similar results were also obtained for Bi_2O_3–rGO composites synthesized via microwave-assisted reduction of GO in Bi_2O_3 precursor solution [120].

More recently, quaternary GSNs have also received increasing attention for the photocatalytic breakdown of MB. Chen et al. [103] synthesized γ-Fe_2O_3/SiO_2/graphene/TiO_2 composites by using a simple, environmentally friendly, one-step colloidal blending method. Superior photocatalytic activity under visible light was obtained on the composite system. An increase in graphene content resulted in higher degradation efficiencies of MB. Furthermore, the composite showed very good superparamagnetism, crucial for its recycling and reuse.

4.2. Methyl orange

Methyl orange (MO) is another common dye that has been investigated extensively to evaluate the photocatalytic effectiveness of GSNs for decolorization of colored effluents. MO is a water soluble azo dye and is widely used in textile, printing, paper, food and pharmaceutical industries [126]. The removal of MO from dye-bearing wastewater streams is extremely important due to its toxic, carcinogenic and recalcitrant nature. Table 2 summarizes the photodegradation data of MO by GSNs. It is evident that similar to MB dye, MO is also highly degraded by GSNs when prepared in combination with TiO_2 [80,127,128,134,136–139]. Besides, a recent study by Pastrana-Martínez and colleagues compared the photocatalytic efficiency of GO–TiO_2, CNT–TiO_2, and C_{60}–TiO_2 composites toward MO [150]. Among all the composites tested, GO–TiO_2 featured the highest photocatalytic activity under near-UV/vis and visible light irradiation, which was attributed to the optimal self-assembly between GO and TiO_2 particles, thereby making the composite act simultaneously as an electron donor as well as an acceptor, and hence suppressing charge recombination.

Additionally, graphene/metal oxide nanocomposites have also shown excellent performance for photodegradation of MO. Fu et al. [55] developed $BiVO_4$–graphene ($BiVO_4$–G) photocatalyst by a facile one-step hydrothermal method without the use of any surfactants. The photocatalytic measurements demonstrated that $BiVO_4$–G nanocomposites were more photoactive than pure $BiVO_4$ photocatalysts for degradation of MO. Almost 99% of the dye was degraded by the $BiVO_4$–G nanocomposite after about 300 min exposure to visible light. Song et al. [84] studied the photocatalytic degradation of MO under visible light irradiation in the presence of BiOBr/graphene nanocomposites. The experimental results showed that the photodecolorization efficiency of the composite photocatalyst was significantly higher than that of commercial P25 catalyst. Liu et al. [129] successfully synthesized a BiOI–graphene composite photocatalyst and used it to degrade MO under visible light irradiation. GO/BiOI and rGO/BiOI nanocomposites have also

Table 2
Photocatalytic degradation of MO by GSNs in aqueous solutions.

Photoactive nanocomposite	Initial dye conc.	Catalyst dose ($g\,L^{-1}$)	Light source	Irradiation time (min)	Degradation (%)	Reference
TiO_2–graphene	20 mg L^{-1}	0.25	UV	30	95	[127]
TiO_2/graphene	5.0×10^{-5} M	–	Visible	60	100	[128]
$BiVO_4$–graphene	20 mg L^{-1}	0.5	Visible	300	99	[55]
$CoFe_2O_4$–graphene	20 mg L^{-1}	0.25	Visible	240	71	[56]
WO_3@graphene	0.025 g L^{-1}	1	Simulated sunlight	120	92.7	[50]
BiOBr/graphene	7.5 mg L^{-1}	0.2	Visible	140	>80	[84]
BiOI–graphene	10 mg L^{-1}	1	Visible	240	88	[129]
ZnO/graphene	20 mg L^{-1}	1	Visible	90	>65	[45]
CdS–graphene	10 mg L^{-1}	0.3	Visible	300	90	[52]
In_2S_3/graphene	25 mg L^{-1}	1	Visible	120	98	[53]
Graphene–N/TiO_2	10 mg L^{-1}	1	Visible	180	>95	[130]
Graphene–Fe/TiO_2	10 mg L^{-1}	1	Visible	180	>85	[131]
Cu–TiO_2/graphene	10 mg L^{-1}	1	Visible	180	>70	[132]
Graphene–neodymium/TiO_2	10 mg L^{-1}	1	Visible	180	~70	[133]
CdSe–graphene–TiO_2	1.0×10^{-4} M	10	Visible	180	71	[59]
Graphene–TiO_2	10 mg L^{-1}	1	Visible	180	>65	[134]
Ag_3VO_4/TiO_2/graphene	10 mg L^{-1}	1	Visible	180	81	[135]
GO/TiO_2	10 mg L^{-1}	0.5	UV	9	95	[136]
GO–TiO_2	20 mg L^{-1}	0.25	UV	110	96	[80]
GO–TiO_2	3.05×10^{-5} M	0.5	Near-UV/vis	30	~100	[137]
GO–TiO_2	20 mg L^{-1}	0.25	UV	90	95	[138]
GO–P25	3.05×10^{-5} M	0.5	UV/vis	30	100	[139]
GO/BiOI	20 mg L^{-1}	0.5	Visible	180	>80	[140]
CdS/ZnO/GO	1.0×10^{-5} M	4	Visible	60	99	[141]
CdS/Al_2O_3/GO	1.0×10^{-5} M	4	Visible	60	90	[141]
rGO–TiO_2	3.05×10^{-5} M	0.5	Near-UV/vis	30	~100	[142]
Ag_3PO_4/GO	20 mg L^{-1}	0.8	Visible	50	86.7	[48]
Ag_3PO_4/rGO	10 mg L^{-1}	0.29	Visible	210	92	[119]
Ag/AgBr/rGO	–	–	Visible	60	95	[143]
Cu_2O/*n*-propylamine/rGO	30 mg L^{-1}	0.5	Visible	180	95	[144]
ZnO/rGO	15 mg L^{-1}	–	UV	90	94	[145]
rGO/BiOI	20 mg L^{-1}	0.5	Visible	180	99	[140]
Bi_2O_3–rGO	5 mg L^{-1}	2	Visible	240	93	[120]
$Fe_{2.25}W_{0.75}O_4$/rGO	10 mg L^{-1}	0.05	UV	60	92	[146]
α-$SnWO_4$/rGO	20 mg L^{-1}	1	Visible	240	41.2	[147]
Au/rGO–TiO_2	20 mg L^{-1}	–	Simulated sunlight	140	100	[148]
Ag@Ag_3PO-/rGO	12 mg L^{-1}	2	Visible	18	97	[149]

been reported for the photodegradation of MO in aqueous phase [140]. However, the photocatalytic efficiency of GO/BiOI was found to be considerably lower than that of rGO/BiOI (Fig. 6). Recently, Bi_2O_3–rGO composites have also been reported as an excellent new photocatalyst for textile wastewater treatment [120]. A high MO degradation rate of up to 93% could be achieved under visible light irradiation for 240 min.

Zhou et al. [50] investigated the feasibility of WO_3 nanorods@graphene to degrade MO under simulated sunlight.

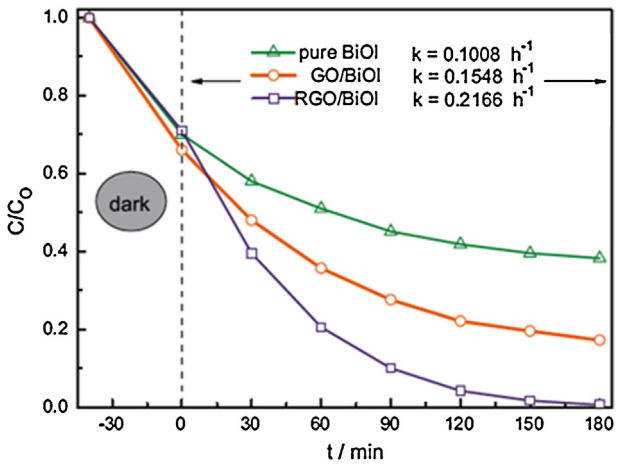

Fig. 6. Degradation of MO under visible-light illumination (λ > 420 nm) with pure BiOI, GO/BiOI, and rGO/BiOI. Reprinted from [140], Copyright 2012, with permission from Elsevier.

The nanocomposite exhibited a significantly higher photocatalytic activity than bare WO_3 nanorods. The authors explained that the presence of graphene increased the charge transport and separation of photogenerated charge carriers, thereby increasing the photocatalytic efficiency. Huang et al. [147] synthesized α-$SnWO_4$/rGO nanocomposite through a facile one-pot hydrothermal reaction between GO, $SnCl_2{\cdot}2H_2O$ and $(NH_4)_5H_5[H_2(WO_4)_6]{\cdot}H_2O$. In comparison to pure α-$SnWO_4$, the decomposition rate of MO by α-$SnWO_4$/rGO was significantly higher due to inhibition of the photogenerated charge carrier recombination process by rGO. Recently, Sarkar and Basak [145] prepared ZnO/rGO hybrids by a one-step hydrothermal method without using any harmful or toxic reducing agent. The photocatalytic activity for the decomposition of MO was investigated under UV light irradiation for 180 min and a degradation efficiency of 94% could be achieved. Similar photoactivity trend for degradation of MO by rGO/ZnO composites has also been observed by Zhang et al. [151].

In an interesting study by Guo et al. [146], $Fe_{2.25}W_{0.75}O_4$/rGO composites were synthesized by a simple one-pot hydrothermal method, employing GO, sodium tungstate (Na_2WO_4), ferrous sulfate ($FeSO_4$) and sodium dodecyl benzenesulfonate (SDBS) as the precursors. The composite displayed a largely improved photocatalytic performance for degradation of MO compared with pure $Fe_{2.25}W_{0.75}O_4$ under low-power UV irradiation due to the introduction of rGO. The composite photocatalyst could also be reused for multiple cycles due to its good thermal stability. Moreover, because of its excellent magnetic properties, $Fe_{2.25}W_{0.75}O_4$/rGO merits further consideration for photocatalytic elimination of environmental pollutants.

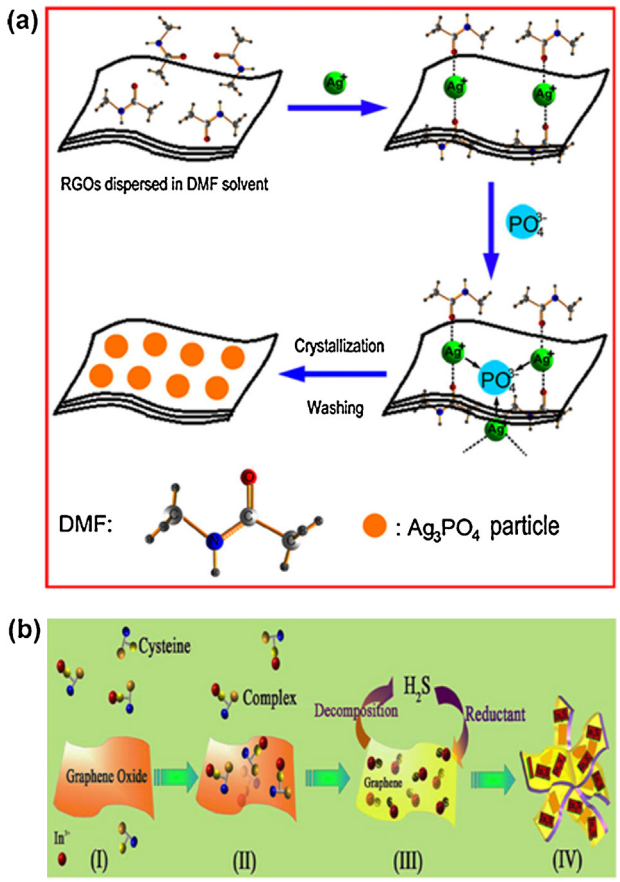

Fig. 7. (a) Illustration of the synthesis of Ag_3PO_4/rGO nanocomposites. Reprinted from [119], Copyright 2012, with permission from Elsevier. (b) A schematic diagram for the different synthesis steps of In_2S_3/G composites. Stage I: A coordination complex is formed between In^{3+} and —SH of cysteine because of their stronger interactions; Stage II: The complex is self-anchored on the surface of GO sheets through interaction between the functional groups of cysteine (—COOH, —NH_2) and GO (—OH, —COOH, C—O—C); Stage III: During hydrothermal treatment, the splitting of S—C bonds results in the formation of In_2S_3 nuclei and releases H_2S which in turn reduces GO to rGO; Stage IV: Partial overlap or coalescence of rGO sheets results in the formation of the final 3D cross-linked architecture. Reprinted from [53], Copyright 2012, with permission from Elsevier.

Recently, Ag_3PO_4, a promising visible light driven photocatalyst for the oxidation of water and photodecomposition of some organic compounds [119], has also been coupled with graphene nanomaterials for improved photocatalytic performance toward decomposition and mineralization of MO. Chen et al. [103] constructed Ag_3PO_4/GO composite by a liquid phase deposition method. The as-prepared composite, with GO content of 15 wt.%, exhibited superior activity under visible light irradiation. The degradation rate constant of MO removal by Ag_3PO_4/GO was 17.9 times higher than that of pure Ag_3PO_4. Dong et al. [119] synthesized Ag_3PO_4/rGO nanocomposites by a facile chemical precipitation approach in *N*,*N*-dimethylformamide (DMF) solvent without any hard/soft templates (Fig. 7a). The photocatalytic activity of pure Ag_3PO_4 nanoparticles was enhanced (3 times) following attachment to rGO sheets.

Some metal sulfides have also been considered for the fabrication of graphene-based photocatalysts for decolorization of MO in aqueous suspensions, due to their narrow band gap and proper band potentials [152]. For example, Pan and Liu [52] prepared CdS nanoparticles/graphene (CdS/G) nanocomposites via a hydrothermal method. After 300 min exposure to visible light, the CdS/G composite was able to degrade up to 90% of the dye. An et al. [53] developed In_2S_3 nanosheets/graphene (In_2S_3/G) composites through a cysteine-assisted one-pot hydrothermal reaction (Fig. 7b). The results of MO degradation studies showed that the photodegradation rate of In_2S_3/G was almost 5 times higher than that of In_2S_3 nanosheets under visible light illumination. In_2S_3/G nanocomposites fabricated at the temperature of 180 °C showed much higher photoactivity than those synthesized at 150 °C or 200 °C. Moreover, a cysteine/In^{3+} ratio of 3 was found beneficial for the superior photocatalytic efficiency. To further illustrate the strong photocatalytic ability of In_2S_3/G, the decomposition of MO over several other common photocatalysts, including Ag_3PO_4, graphene/CdS nanorods (G/CdS NRCs) composites and nitrogen doped TiO_2 (N–TiO_2, was also studied. Under visible light irradiation, the photocatalytic degradation rate followed the order In_2S_3/G > Ag_3PO_4 > G/CdS NRCs > N–TiO_2.

In addition to binary nanocomposites, ternary hybrids have also been largely explored to develop novel photocatalysts with high activity for MO in the visible light region. Ghosh et al. [59] fabricated CdSe–graphene–TiO_2 (CdSe–G–TiO_2) ternary hybrids by calcination of CdSe–graphene composites with titanium (IV) *n*-butoxide as the source of TiO_2 at 600 °C. After 180 min of exposure to visible light, about 71% of MO was mineralized by the as-synthesized CdSe–G–TiO_2 nanocomposites. In addition, there was no significant decrease in the photocatalytic activity of CdSe–G–TiO_2 even after four recycles. The photodegradation followed first-order kinetics with a reaction rate constant of 0.0041 min^{-1}. Wang et al. [135] studied the effectiveness of Ag_3VO_4/TiO_2/graphene (Ag_3VO_4/TiO_2/G) nanocomposite for the degradation of MO under visible light illumination. The Ag_3VO_4/TiO_2/G composite exhibited a significantly higher photocatalytic activity than Ag_3VO_4/TiO_2 or TiO_2/G composites as well as Ag_3VO_4, nitrogen doped TiO_2 and commercial Degussa P25. The enhanced photoactivity of Ag_3VO_4/TiO_2/G was attributed to the combined effect of formation of hetero-junction between Ag_3VO_4 and TiO_2, electron storage and shuttling ability of graphene and also its wide spectral response.

It is well known that TiO_2 is the most widely used photocatalyst in environmental pollution control and abatement because it has a strong oxidation ability, superhydrophilicity, chemical stability, and is non-toxic, inexpensive and transparent to visible light [153,154]. However, a major constraint in the practical application of TiO_2 is its limited optical absorption and recombination of photogenerated e^-/h^+ pairs which result in low activity [116]. An attractive method to improve the photocatalytic efficiency of TiO_2 is doping with metals (e.g., Cu, Cr, Fe, Mn, Mo, Ca, Ce, Sr, Ba, La, Er and V) or non-metals (e.g., N, C, S, B, P and F) [12,131]. Another common approach for enhancing the photocatalytic efficiency of TiO_2 is immobilization of TiO_2 nanoparticles on conjugated carbon materials such as graphite, fullerene or graphene [152]. Khalid and co-workers [130–133] combined both the approaches and synthesized a variety of X-doped TiO_2 nanoparticles (X = N, Fe, Cu, Nd) anchored on graphene sheets. The resulting G–X/TiO_2 ternary composites were tested for the degradation of MO under visible irradiation. The degradation efficiency of TiO_2 was enhanced by doping and introduction of graphene into the composites. The photocatalytic activity was in the order G–N/TiO_2 > G–Fe/TiO_2 > G–Cu/TiO_2 > G–Nd/TiO_2. The photocatalytic decomposition of MO by G–X/TiO_2 nanocomposites followed the pseudo-first-order reaction kinetics with rate constants of 1.54×10^{-2}, 0.72×10^{-2}, 0.77×10^{-2}, and 0.68×10^{-2} min^{-1} for G–N/TiO_2, G–Fe/TiO_2, G–Cu/TiO_2 and G–Nd/TiO_2, respectively [130–133].

Khan et al. [141] examined the visible-light-induced photocatalytic activity of CdS/Al_2O_3/GO and CdS/ZnO/GO composites, prepared by a one-pot hydrothermal method, for degradation of MO. Under identical experimental conditions, both the composites were found to be efficient for degradation of MO in aqueous suspensions (90% for CdS/Al_2O_3/GO and 99% for CdS/ZnO/GO within

60 min of visible light illumination). Chen et al. [148] prepared Au/rGO co-loaded TiO_2 nanotube hybrids by a simple electrodeposition method. Compared with Au–TiO_2, rGO–TiO_2, and unmodified TiO_2, Au/rGO–TiO_2 exhibited enhanced photocatalytic activity in the degradation of MO under simulated solar light illumination, which was due to increased photoresponse both in the UV and in the visible region, high electron–hole separation efficiency, and improved adsorptivity toward dye molecules, resulting from the synergetic effects of TiO_2, rGO and Au nanoparticles. Luo et al. [155] fabricated a Ag/AgCl/rGO heterostructure photocatalyst via a hydrothermal method that exhibited higher visible light activity toward MO than Ag/AgCl composites alone. In quite similar studies, Ag/AgBr/rGO and Ag@Ag_3PO_4/rGO ternary nanocomposites have also been demonstrated to efficiently degrade MO under visible light irradiation [143,149].

Recently, Cu_2O/PA/rGO prepared by immobilization of Cu_2O nanoparticles on *n*-propylamine (PA) intercalated GO sheets via a coordination strategy showed excellent performance to photodegrade MO [144]. A degradation efficiency of 95% was recorded following exposure to visible light for 180 min. The introduction of organic functional groups on graphitic sheets not only improved the surface accessibility of the graphene sheets, but also increased the surface area of the resultant composites. In addition, the uniform distribution of Cu_2O nanoparticles effectively decreased the charge-transfer resistance of the composite by arresting the restacking of the graphitic sheets. Together, these factors were responsible for the high visible photocatalytic activity of Cu_2O/PA/rGO.

4.3. Rhodamine B

Rhodamine B (RhB) is a water-soluble fluorescent xanthene dye, widely used in textile industries for dyeing cotton, wool, and silk [156–158]. The dye is, however, potentially toxic and carcinogenic to humans and animals and can cause irritation to the skin, eyes, gastrointestinal and respiratory tracts [156,158]. Considering its hazardous and detrimental effects on human and aquatic life, RhB is often studied as a model dye pollutant for photocatalytic degradation by GSNs (Table 3). As can be seen in Table 3, RhB is effectively photodegraded by GSNs synthesized by coupling common semiconductor solid particles such as TiO_2 [135,163,164,169,170], P25 [163], ZnO [86,117], Mn_2O_3 [49], Ag_3PO_4 [103], CdS [90,159], and Sb_2S_3 [54]. In addition, many other types of GSNs have also been developed and tested for photodegradation of RhB; their characteristics and performance are discussed in the following paragraphs.

Tu et al. [160] reported the complete decolorization of RhB solutions by visible light induced BiOBr–graphene composites, prepared through a facile in situ solvothermal method. Ma and co-workers fabricated a Bi_2WO_6/graphene composite that showed excellent photocatalytic activity for the degradation of RhB under both UV and visible light irradiation [171]. Min et al. [161] synthesized nanosized bismuth niobate ($Bi_5Nb_3O_{15}$) by a facile hydrothermal method, which were then self-assembled onto graphene sheets to prepare $Bi_5Nb_3O_{15}$/graphene ($Bi_5Nb_3O_{15}$/G) nanocomposites. The photocatalytic decolorization ratio of the nanosized $Bi_5Nb_3O_{15}$ for RhB was remarkably improved (2.8 times) after coupling with graphene. The novel $Bi_5Nb_3O_{15}$/G composite was also found to have higher photodecolorization efficiency for RhB compared to Degussa P25. Moreover, the composite also did not show any change in decolorization efficiency even after recycle and reuse for five consecutive cycles.

Bai et al. [116] fabricated a series of rGO–MFe_2O_4 (M = Mn, Zn, Co and Ni) hybrids by a one-pot solvothermal method, which were then examined for the visible light decomposition of RhB. The photocatalytic activity of the different rGO–MFe_2O_4 hybrids decreased in the following order: rGO–$CoFe_2O_4$ > rGO–$ZnFe_2O_4$ > rGO–$MnFe_2O_4$ > rGO–$NiFe_2O_4$. Recently, Li et al. [174] prepared reduced graphene oxide/potassium niobate (rGO/$KNbO_3$) composite nanoscrolls by incorporating reduced rGO sheets into $KNbO_3$ sheets at room temperature. The rGO/$KNbO_3$ composite nanoscroll exhibited a moderate RhB degradation efficiency of 68.3% after UV irradiation for about 30 min.

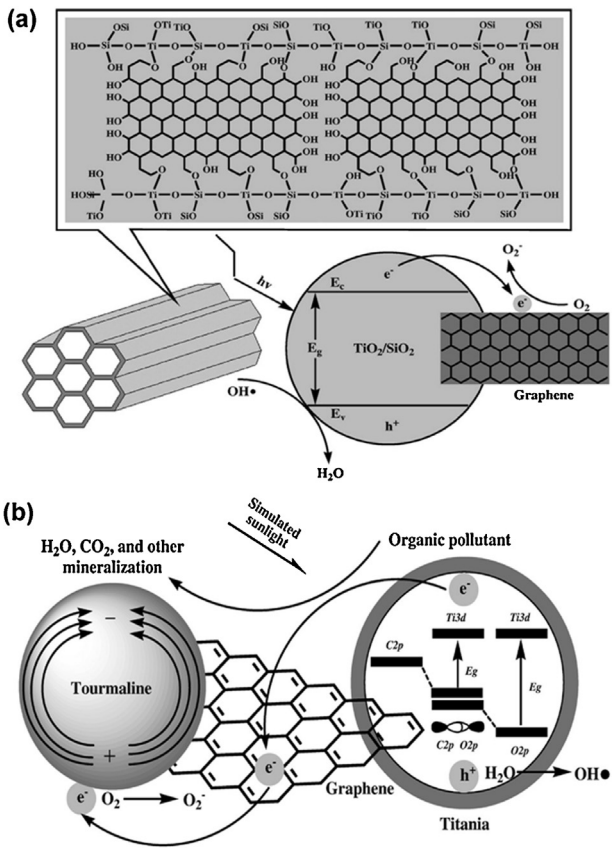

Fig. 8. (a) Wall structure and photocatalytic cycle of ordered mesoporous graphene–titania/silica composite material. Reprinted from [74], Copyright 2012, with permission from Elsevier (b) Transport and capture of photogenerated electrons in the graphene and tourmaline co-doped titania three-component system. Reprinted from [74], Copyright 2012, with permission from Elsevier.

Besides, a number of ternary nanocomposites have been recently developed and tested for the photodegradation of RhB in liquid phase (Table 3). Li et al. [73] prepared a chemically bonded graphene–titania/silica (G-TiO_2/SiO_2) nanocomposite with hexagonal ordered mesoporous structure as illustrated in Fig. 8a. The photocatalytic performance of the G-TiO_2/SiO_2 nanocomposite was superior to that of TiO_2/SiO_2 composites. The G-TiO_2/SiO_2 composite photocatalyst completely decomposed RhB within 30 min of exposure to simulated sunlight. The exceptional photocatalytic performance of G-TiO_2/SiO_2 was attributed to the following: the incorporation of graphene within TiO_2/SiO_2 composite resulted in enhanced quantum efficiency. Graphene served as an acceptor of the photogenerated electrons from TiO_2/SiO_2 composite and effectively suppressed the e^-/h^+ pair recombination, leaving more photogenerated holes to form reactive species, thereby augmenting the photodegradation of RhB (Fig. 8a). Furthermore, the surface defects of TiO_2 lattices trapped the charge carriers and transferred them to the reactants, thus, enhancing the quantum efficiency of the photocatalyst. In addition, the ordered mesoporous structure and perfect surface textural properties also contributed to improving the photocatalytic activity of the photocatalyst by facilitating the accessibility to the active sites in the framework. In

Table 3
Photocatalytic degradation of RhB by GSNs in aqueous solutions.

Photoactive nanocomposite	Initial dye conc.	Catalyst dose ($g\,L^{-1}$)	Light source	Irradiation time (min)	Degradation (%)	Reference
$BiVO_4$–graphene	$20\,mg\,L^{-1}$	0.5	Visible	300	99	[55]
$CoFe_2O_4$–graphene	$20\,mg\,L^{-1}$	0.25	Visible	240	94	[56]
Graphene–Mn_2O_3	1.2×10^{-5} M	0.5	UV	60	60	[49]
Graphene–CdS	1.0×10^{-5} M	0.4	Visible	80	95	[159]
Graphene–TiO_2/silica	$10\,mg\,L^{-1}$	1	Simulated sunlight	30	100	[73]
BiOBr–graphene	$10\,mg\,L^{-1}$	0.2	Visible	24	100	[160]
$Bi_5Nb_3O_{15}$/graphene	1.0×10^{-5} M	0.6	Visible	80	>80	[161]
ZnO–graphene	$40\,mg\,L^{-1}$	0.71	UV	60	100	[162]
Graphene/P25	$10\,mg\,L^{-1}$	0.3	Visible	40	96	[163]
Graphene/TiO_2	$10\,mg\,L^{-1}$	0.3	Visible	40	97	[163]
Graphene/TiO_2	$20\,mg\,L^{-1}$	1	Simulated sunlight	60	>90	[164]
CdSe–graphene–TiO_2	1.0×10^{-4} M	10	Visible	180	85	[59]
Graphene–tourmaline–TiO_2	$20\,mg\,L^{-1}$	1	Simulated sunlight	60	>60	[74]
Ag_3VO_4/TiO_2/graphene	$10\,mg\,L^{-1}$	1	Visible	40	100	[135]
Ag_3VO_4/TiO_2/graphene	$10\,mg\,L^{-1}$	1	Simulated sunlight	25	100	[135]
Bi_2O_3/TiO_2/graphene	1.0×10^{-5} M	2	Visible	50	99.7	[165]
ZnO/Ag/graphene	$20\,mg\,L^{-1}$	0.4	UV	50	100	[166]
Graphene-Sb_2S_3	$10\,mg\,L^{-1}$	0.4	Visible	120	89	[54]
Ag_3PO_4/GO	$20\,mg\,L^{-1}$	0.8	Visible	30	100	[48]
Ti/Ce–GO	10^{-5} M	0.16	Visible	240	~70	[167]
Au@Mo–GO	$10\,mg\,L^{-1}$	–	Visible	120	80	[87]
GO–CdS	$20\,mg\,L^{-1}$	0.4	Visible	60	>90	[90]
rGO–Au	5.3×10^{-3} M	0.063	Visible	<225	>70	[168]
rGO–TiO_2	–	–	Visible	120	>60	[169]
rGO–TiO_2	–	–	UV	120	>90	[169]
rGO–TiO_2	2.0×10^{-5} M	0.2	UV	120	80-90	[170]
rGO/TiO_2	0.5×10^{-5} M	–	UV	30	~100	[171]
TiO_2–dx–rGO	$5\,mg\,L^{-1}$	0.2	UV	<60	>90	[172]
rGO/Bi_2WO_6	10^{-5} M	1	Visible	40	98	[173]
rGO/Bi_2WO_6	10^{-5} M	1	UV	75	98	[173]
rGO–$CoFe_2O_4$	$10\,mg\,L^{-1}$	0.16	Visible	180	>85%	[116]
rGO/$KNbO_3$	5.0×10^{-5} M	1	UV	30	68.3	[174]
rGO/ZnO	$10\,mg\,L^{-1}$	0.125	Visible	40	>95	[86]
Ag/AgBr/rGO	1.0×10^{-5} M	0.5	Visible	30	87	[64]

another study, Li et al. [74] found that graphene–tourmaline–TiO_2 (G–T–TiO_2) composites displayed a higher photocatalytic activity than pure TiO_2 for degradation of RhB under simulated sunlight irradiation. As shown in Fig. 8b, graphene, owing to its excellent electrical conductivity, rapidly transported the photogenerated electrons from the CB of TiO_2 to tourmaline, resulting in the reduction of e^-/h^+ pair recombination and thus improved photocatalytic activity.

Another important investigation that deserves special mention is the preparation of TiO_2–dextran–rGO composites by an environmentally friendly and efficient strategy for photodegradation of RhB (Fig. 9) [172]. In this study, GO was first reduced to rGO by using dextran as reducing agent and a surface modifier. TiO_2 nanoparticles were then successfully prepared from a water soluble precursor, peroxotitanium acid and self-assembled on dx–rGO nanosheets through hydrogen bonding and van der Waals interactions. Compared with TiO_2, the TiO_2–dx–rGO composite exhibited remarkably enhanced photocatalytic performance for degradation of RhB under UV irradiation. The integration of rGO into the matrix of TiO_2 not only increased the light absorption intensity but also improved the adsorptivity of the dye pollutant. RhB molecules could transfer from the solution to the catalyst surface and be adsorbed with offset face-to-face orientation via π–π conjugation between dye and aromatic regions of rGO. Also, the large surface area of rGO offered adequate active sites to participate in photocatalysis, which ultimately enhanced the photocatalytic activity of TiO_2.

Recently, several other ternary nanocomposites including Bi_2O_3/TiO_2/graphene [165], ZnO/Ag/graphene [166], Ti/Ce–GO [167], Au@Mo–GO [87] and Ag/AgBr/rGO [64] have also been developed and tested for photodegradation of RhB with varying levels of success.

4.4. Other dyes

GSNs as a new type of photocatalyst have also been extensively investigated for the degradation and mineralization of other common dyes (Table 4). For instance, Wang et al. [175] demonstrated the synthesis of graphene–Bi_2MoO_6 (G–Bi_2MoO_6) nanocomposite by a one-pot solvothermal method and tested its photocatalytic performance for the degradation of Reactive Brilliant Red X-3B dye under visible light irradiation. Nearly 90.4% degradation of X-3B was achieved after 90 min irradiation, whereas only 63.8% degradation was obtained using pure Bi_2MoO_6 for the same time. The variation in degradation efficiency was attributed to increased migration efficiency of photo-induced electrons as well as increased adsorption affinity owing to the presence of graphene. The degradation process of X-3B followed first-order reaction kinetics with a rate constant of $0.022\,min^{-1}$. Zhang et al. [162] prepared graphene/BiOBr (G/BiOBr) composites by a typical hydrothermal reaction between GO and BiOBr. The presence of graphene on the surface of BiOBr significantly improved the photocatalytic activity of the bulk material for the degradation of Sulforhodamine 640 (Srh 640) dye under visible light irradiation (Fig. 10a). The photocatalytic efficiency of BiOBr was enhanced because of the low isoelectric characteristics of graphene and better interfacial electron transfer between BiOBr and graphene. The pseudo-first-order kinetic model was applied to study the photocatalytic kinetics of Srh 640. The high correlation coefficient values ($R^2 > 0.99$) obtained by linear regression analysis, confirmed that the photodecomposition process was kinetically controlled by a pseudo-first-order rate law (Fig. 10b). The rate constants for removal of Srh 640 in presence of pure BiOBr and G/BiOBr composites were found to be $0.004\,min^{-1}$ and $0.00798\,min^{-1}$, respectively.

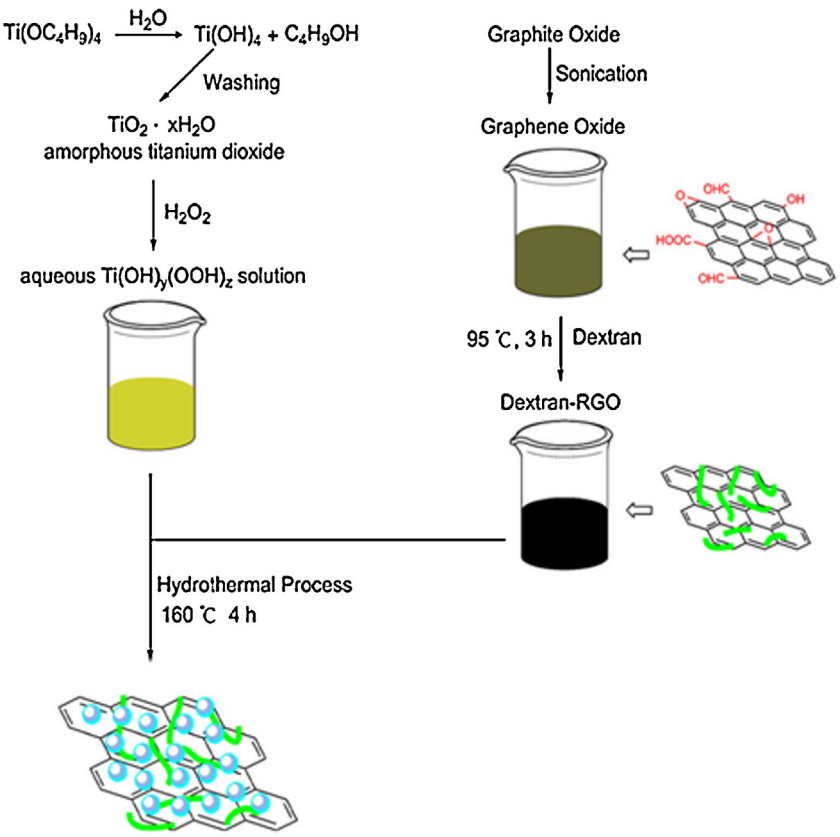

Fig. 9. Protocol for the fabrication of TiO_2–dx–rGO nanocomposites. Reprinted from [172], Copyright 2012, with permission from Elsevier.

Fu et al. [56] found that $CoFe_2O_4$–graphene ($CoFe_2O_4$–G) nanocomposites fabricated by a facile one-step hydrothermal method were highly efficient and stable than pure $CoFe_2O_4$ for visible light-induced decomposition of Active Black BL-G and Active Red RGB dyes. The increased photoactivity of $CoFe_2O_4$–G was related to the reduction of GO, since the excellent conductivity of the reduced GO sheets was favorable for the efficient separation of photogenerated carriers in the $CoFe_2O_4$ and graphene coupling system. Chandra et al. [49] investigated the photocatalytic potential of graphene–Mn_2O_3 composites to degrade Eosin. A removal efficiency of 80% was observed within 140 min of UV irradiation. He et al. [108] demonstrated that ZnO–Bi_2O_3/GO is a very efficient

Table 4
Photocatalytic degradation of various other dyes by GSNs in aqueous solutions.

Dye	Photoactive nanocomposite	Initial dye conc.	Catalyst dose ($g\,L^{-1}$)	Light source	Irradiation time (min)	Degradation (%)	Reference
Active Black BL-G	$BiVO_4$–graphene	20 mg L^{-1}	0.5	Visible	300	99	[55]
Active Black BL-G	$CoFe_2O_4$–graphene	20 mg L^{-1}	0.25	Visible	240	66	[56]
Active Red RGB	$CoFe_2O_4$–graphene	20 mg L^{-1}	0.25	Visible	240	61	[56]
Reactive Brilliant Red X-3B	Graphene–Bi_2MoO_6	25 mg L^{-1}	0.5	Visible	90	90.4	[175]
Reactive Black 5	P25–graphene	10 mg L^{-1}	0.4	UV	100	>90	[101]
Reactive Black 5	Ag–ZnO/rGO	10 mg L^{-1}	0.66	UV	200	>80	[176]
Reactive Red 195	CeO_2–TiO_2–graphene	20 mg L^{-1}	0.08	UV	100	~90	[177]
Reactive Red 195	Pt–TiO_2–graphene	20 mg L^{-1}	0.08	UV	120	>75	[178]
Reactive Red 195	Pd–TiO_2–graphene	20 mg L^{-1}	0.08	UV	120	>60	[178]
Rose Bengal	Graphene/polyaniline	–	2	Visible	180	56	[179]
Sulforhodamine 640	Graphene/BiOBr	10 mg L^{-1}	0.5	Visible	60	34.8	[180]
Eosin	Graphene–Mn_2O_3	2.5×10^{-5} M	0.5	UV	140	80	[49]
Acid Orange 7	TiO_2–Graphene	30 mg L^{-1}	0.36	UV	90	99.99	[181]
Acid Orange 7	GO–TiO_2 nanorod	100 mg L^{-1}	–	UV	30	73	[182]
Acid Orange 7	GO–TiO_2 nanoparticle	100 mg L^{-1}	–	UV	30	94	[182]
Acid Orange 7	GO–Ag_3PO_4	50 mg L^{-1}	0.4	UV	10	100	[183]
Acid Orange 7	GO–CdS	20 mg L^{-1}	0.4	Visible	60	>80	[90]
Crystal Violet	ZnO–GO	–	2	UV	80	~95	[184]
Malachite Green	ZnO–rGO	6.0×10^{-5} M	0.5	UV	90	78	[43]
Acid Blue	ZnO–Bi_2O_3/GO	10 mg L^{-1}	0.5	Visible	120	98.31	[108]
Acid Yellow	ZnO–Bi_2O_3/GO	10 mg L^{-1}	0.5	Visible	120	88.69	[108]
Acid Red	ZnO–Bi_2O_3/GO	10 mg L^{-1}	0.5	Visible	120	81.93	[108]
Reactive Blue	ZnO–Bi_2O_3/GO	10 mg L^{-1}	0.5	Visible	120	44.23	[108]
Reactive Yellow	ZnO–Bi_2O_3/GO	10 mg L^{-1}	0.5	Visible	120	80.28	[108]
Reactive Red	ZnO–Bi_2O_3/GO	10 mg L^{-1}	0.5	Visible	120	85.35	[108]

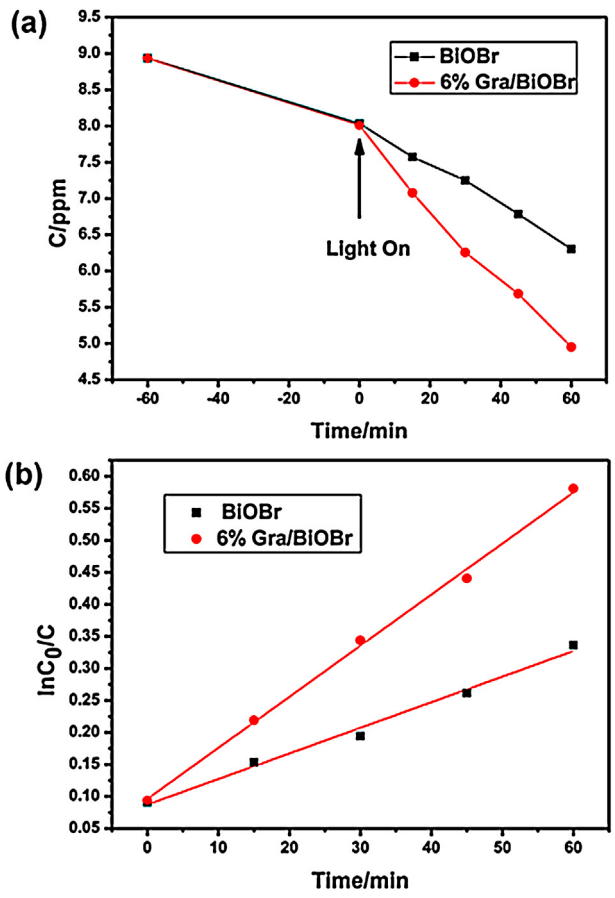

Fig. 10. (a) Extent of photocatalytic degradation of Srh 640 using graphene/BiOBr nanocomposites and pure BiOBr as a function of irradiation time (b) Pseudo-first-order kinetic plots for photodecomposition of Srh 640. Reprinted from [162], Copyright 2012, with permission from Elsevier.

visible light sensitive photocatalyst capable of degrading a variety of textile dyes (such as Acid Blue, Acid Yellow, Acid Red, Reactive Blue, Reactive Yellow, and Reactive Red). Recently, Li et al. [101] constructed P25-graphene (P25-G) nanocomposites with high specific surface area and narrow band gap energy that were much more efficient for the UV light degradation of Reactive Black 5 (RB5) than Degussa P25. Upon 100 min UV irradiation, >90% photodegradation of RB5 was observed with P25–G.

Ghasemi and co-workers [177] evaluated the photodecomposition of Reactive Red 195 (RR 195) under UV light illumination by TiO_2 and CeO_2–TiO_2 (CT) nanoparticles, and CeO_2–TiO_2–carbon nanotubes (CT–CNTs), CeO_2–TiO_2–activated carbon (CT–AC) and CeO_2–TiO_2–graphene (CT–G) nanocomposites. The order of photocatalytic efficiency was TiO_2 < CT < CT–AC < CT–CNTs < CT–G. The CT–G nanocomposite demonstrated the highest photocatalytic activity due to its unique structure and unprecedented electronic properties. Interestingly, the photocatalytic activity of CT–G was found to be inversely proportional to the graphene content in the nanocomposite. In another recent study, Ghasemi et al. [178] demonstrated that M–TiO_2–graphene (M–TiO_2–G; M = Pt, Pd) composites can also efficiently degrade RR 195 under both UV and visible light irradiation. However, the photocatalytic activity under UV light was much higher than visible light. The visible-light irradiation with $\lambda > 400$ nm did not had sufficient energy to excite the VB electrons in high extent, resulting in lesser number of excited electrons and hence lower degradation compared to UV light. Meanwhile, the photoactivity of Pt–TiO_2–G was found to be higher than that of Pd–TiO_2–G due to high photonic efficiency of the nanocomposite.

Polyaniline/graphene (PANI–G) nanocomposites, prepared through polymerization of aniline monomer with graphene under in situ conditions (Fig. 11), were evaluated for the photodecolorization of Rose Bengal (RB) dye by Ameen et al. [179]. PANI–G nanocomposite efficiently degraded RB dye by 56% within 180 min under visible light illumination. The photocatalytic activity of PANI–G was also much superior to that of pristine PANI. The enhancement in photocatalytic activity was ascribed to the increased e^-/h^+ pair charge separation and the formation of oxyradicals ($\bullet O_2^-$, $\bullet HO_2$, $\bullet OH$) due to the large surface of the nanocomposite provided by graphene sheets. The same research group, recently, investigated the photocatalytic degradation of Crystal Violet by ZnO–GO nanohybrids [184]. An enormously high photodegradation of ~95% was achieved within 80 min of UV irradiation.

Liu et al. [182] studied the comparative efficacy of GO–TiO_2 nanorod composites (GO–TiO_2 NRCs) and GO–TiO_2 nanoparticle composites (GO–TiO_2 NPCs) for the photocatalytic removal of Acid Orange 7 (AO 7) from its aqueous solution under UV irradiation. The results of photocatalytic degradation studies showed that the photocatalytic activity of GO–TiO_2 NRCs was higher than that of GO–TiO_2 NPCs, and up to 94% removal could be achieved after about 30 min of irradiation. The nanocomposites were further tested for the photocatalytic disinfection of water infected with *Escherichia coli*. The GO–TiO_2 NRCs exhibited superior antibacterial activity. *E. coli* cells (at a concentration of 1.7×10^8 cfu mL^{-1}) were completely inactivated by GO–TiO_2 NRCs under solar irradiation within 120 min (Fig. 12). The higher photocatalytic activity of GO–TiO_2 NRCs was due to anti-charge recombination and more {1 0 1} facets. It is interesting to note that the ratio of TiO_2 and

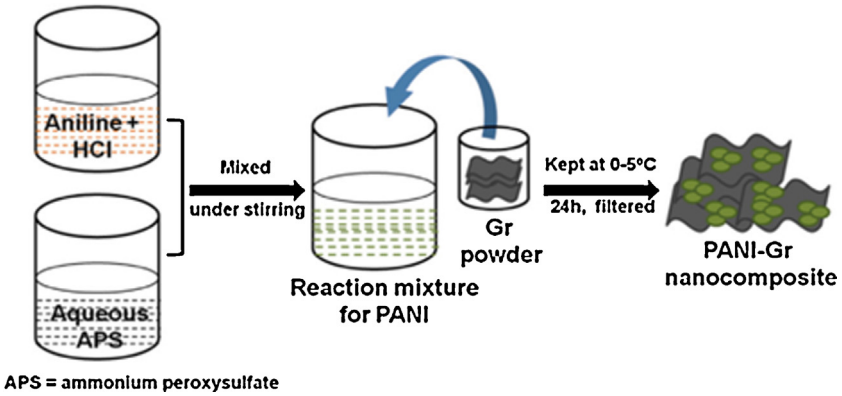

Fig. 11. Schematic of the preparation of PANI-G nanocomposites by in situ polymerization of aniline monomer and graphene sheets. Reprinted from [179], Copyright 2012, with permission from Elsevier.

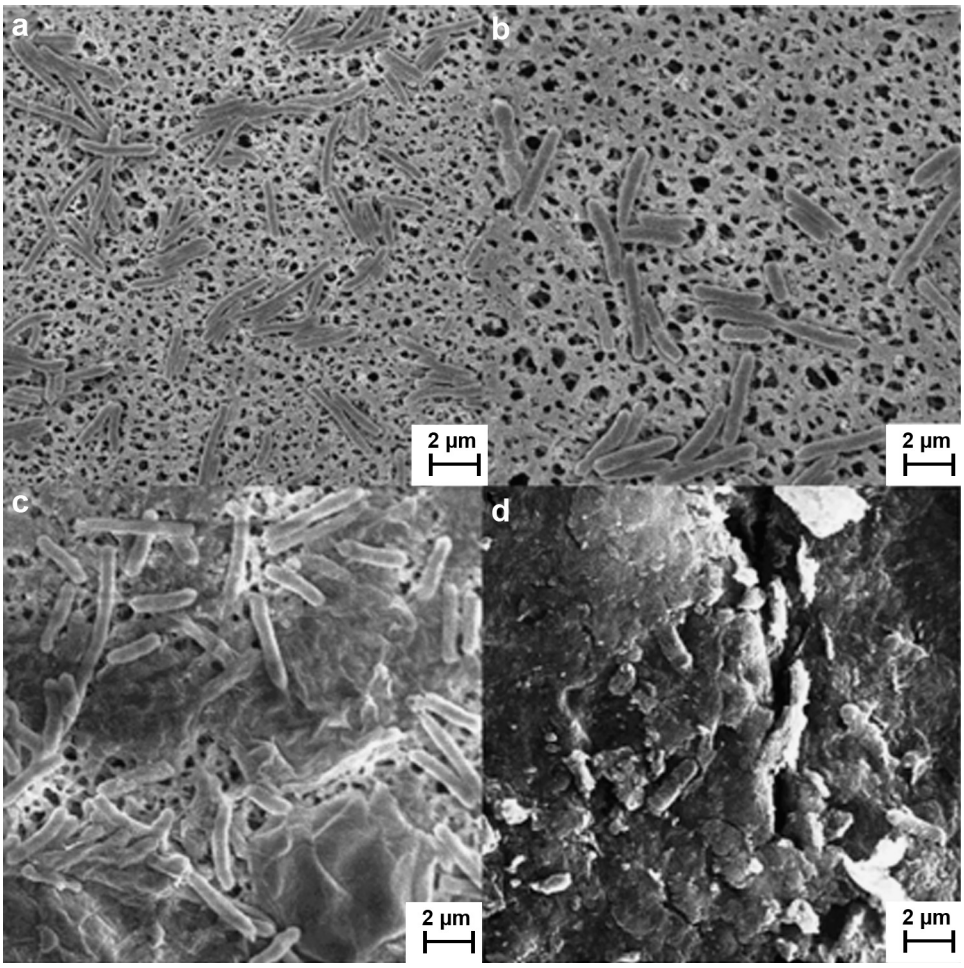

Fig. 12. SEM images of *E. coli* (a) before solar irradiation in absence of GO–TiO_2 NRCs (b) after solar irradiation for 2 h in absence of GO–TiO_2 NRCs (c) before solar irradiation in presence of GO–TiO_2 NRCs (d) after solar irradiation for 2 h in presence of GO–TiO_2 NRCs Reprinted from [182], Copyright 2011, with permission from Elsevier.

GO had no significant effect on the photocatalytic activity of GO–TiO_2 NRCs. In another separate study, Liu et al. [183] found that GO–Ag_3PO_4 composites, fabricated by an ion-exchange method of silver acetate (CH_3COOAg) and disodium phosphate (Na_2HPO_4) in the presence of GO sheets, induced complete decomposition of AO 7 under visible light irradiation. The GO–Ag_3PO_4 composite also showed exceptional intrinsic antibacterial activity toward *E. coli* due to the synergistic effects of excellent bactericidal properties of Ag^+, good adsorption capability of GO toward bacterial cells and high photocatalytic performance of Ag_3PO_4. Recently, Liu's group also explored the photodegradation and disinfection activities of GO–CdS composites [90]. Higher photodegradation rate of AO 7 under visible light was exhibited by the composite (>80%) than that by pure CdS nanoparticles (~50%). In addition, nearly 100% of both gram-negative (*E. coli*) and gram-positive (*Bacillus subtilis*) bacteria were killed by the GO–CdS nanocomposite within 25 min of visible light irradiation. The excellent photodegradation and disinfection activities was attributed to the high quantity of •OH radicals generated under visible light irradiation as confirmed by transient photocurrent measurements and radical scavenger investigations.

Herring et al. [43] reported a simple method for the preparation of ZnO–rGO composites by using microwave irradiation of zinc acetate and GO in the presence of a mixture of oleic acid ($C_{18}H_{34}O_2$) and oleylamine ($C_{18}H_{37}N$). Microwave power density and exposure time strongly influenced the growth rate, shape, size, and morphology of ZnO nanocrystals supported on the rGO nanosheets. The as-synthesized ZnO–rGO nanocomposite was studied as a potential photocatalyst for the degradation of a diamino-triphenylmethane dye, Malachite green (MG). The ZnO–rGO nanocomposites were found to be more efficient than pristine ZnO nanopyramids for photodegradation of the dye under UV irradiation. The photocatalytic decomposition of MG by ZnO–rGO obeyed pseudo-first-order kinetics with high degradation rate constant. The superior performance of the nanocomposite was attributed to the efficient charge transfer of the photogenerated electrons in the CB of ZnO to rGO.

More recently, Pant et al. [68] tested Ag–ZnO/rGO composite for the degradation of RB 5 under UV illumination. The Ag–ZnO/rGO nanocomposite showed good activity for the photodecomposition of RB 5. After 200 min of UV irradiation, more than 80% of RB 5 dye was degraded. Pant et al. explained that because of the excellent electron-accepting property of rGO, photoexcited electrons of ZnO were quickly transferred from its CB to the rGO sheets and anchored Ag nanoparticles. This in turn effectively suppressed the recombination of photo-generated charge carriers, leaving more charge carriers to form highly reactive species ($•O_2^-$, •OH) and promoting the degradation of RB 5 (Fig. 13). Similar to the findings of Liu et al. [183], the Ag–ZnO/rGO composite showed excellent intrinsic antibacterial activity toward gram-negative bacteria (*E. coli*).

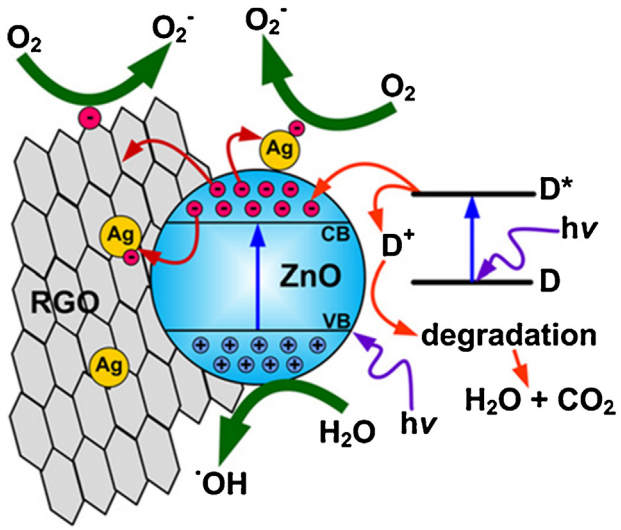

Fig. 13. Proposed mechanism of RB 5 degradation over Ag–ZnO/rGO nanocomposites under UV irradiation (D = dye molecule). Reprinted from [68], Copyright 2012, with permission from Elsevier.

Moreover, the nanocomposite could be recovered easily by sedimentation for repeated use.

5. Conclusion and future perspectives

In this review, an attempt has been made to integrate the recent developments in the synthesis and application of GSNs for photocatalytic treatment of colored effluents. Undoubtedly, GSNs hold great potential for photodegradation of dye pollutants and offer significant advantages over the currently available commercial semiconductor photocatalysts. The incorporation of graphene materials into various semiconductors can significantly improve their photocatalytic performance because of the extended light absorption range, high adsorption capacity, increased specific surface area and superior electron conductivity. Even though considerable progress has been made, there are several key technical issues that need to be further investigated. They are summarized as follows:

(1) It is well known that the initial pH of the reacting medium can significantly influence the photocatalytic degradation rate of dyes, as it affects the surface charge of the photocatalyst material as well as the degree of ionization of the dye molecule. In addition, pH is also directly associated with changes in the structural stability and color intensity of the dye solution [3]. However, in most of the studies reported in the literature, the effect of pH has not been investigated. Also, the effect of other operating parameters such as light intensity, initial dye concentration, photocatalyst dose, oxidizing agents/electron acceptors and the presence of ionic components in solution, on the photocatalytic efficiency of GSNs has been seldom examined.

(2) Optimization of the degradation parameters is compelling from the perspective of designing and development of efficient GSN-based photocatalytic oxidation process. Therefore, the use of advanced statistical optimization tools such as response surface methodology and Taguchi experimental design method is strongly recommended in future research works. These techniques are not only aimed at process optimization and empirical model development, but can also be used to evaluate the relative significance of several process parameters even in the presence of complex interactions.

(3) Not many studies have considered the recycling of the photocatalyst. Regeneration and recycling of GSNs should, therefore, be investigated in detail as they help determine the stability as well as reusability of a photocatalyst, which in turn contributes to evaluating the effectiveness and economic feasibility of the photocatalyst.

(4) It is also evident from the vast literature review that the different synthetic methods available for preparation of GSNs are mainly focused on the dispersion of semiconductor solid particles on the surface of graphene/GO/rGO nanosheets. Such an approach introduces graphene material just for the sake of it without being able to successfully exploit the structural advantages of 2D graphene materials. Taking into account that the main driving force behind the rapid development of GSNs is the urge to combine the outstanding properties of graphene materials with other constituent nanomaterials, more efficient and versatile fabrication methods should, therefore, be developed to make complete utilization of the structural and electronic merits of graphene materials for attaining improved and extraordinary photocatalytic performance.

(5) A direct and systematic comparison of graphene with other carbon nanomaterials (e.g., carbon nanotubes, fullerenes, activated carbon, carbon nanohorns, carbon nanopetals) is also essential to gain a better understanding of the essential merits of graphene as a photocatalyst carrier or promoter, and its potential use for the development of next-generation photocatalyst systems.

(6) Unlike laboratory tests using pure aqueous dye solutions, textile effluents contain different types of synthetic dyes and other undesirable substances. For example, both anionic and cationic dyes may be present simultaneously in real effluents of industrial activities such as paper printing and textile dyeing. It is thus essential to investigate the simultaneous photodecomposition of many co-existing dyes from multicomponent solutions. Further research, in the direction of testing the efficacy of GSNs with real dye-bearing effluents must also be undertaken.

(7) There is an incomplete understanding of the mechanisms of photocatalytic enhancement by GSNs. Thus, more in-depth studies are needed to elucidate the mechanisms of photocatalytic enhancements which in turn would contribute toward designing novel GSNs.

(8) The lack of efficient and low-cost harvesting techniques and inadequate scale-up strategies pose a hindrance to the practical exploitation of GSNs. Therefore, future research work should also aim at addressing these issues.

(9) The cost factor is of utmost importance in determining the selection of the suitable photocatalyst for large scale industrial applications. Low production costs with high photodegradation rates are always preferred as they make the treatment process more economical and efficient. Therefore, cost–benefit analyses of GSNs need to be conducted to study the economic feasibility of applying these promising photocatalysts in treatment of dye-contaminated effluents.

(10) Last but not the least, very little information is currently available in literature on the toxicity and biocompatibility of GSNs. Future investigations should, therefore, concentrate on in vitro and in vivo interactions between GSNs and different living systems to successfully realize the utilization of GSNs in dye–wastewater remediation.

Upon overcoming the above-mentioned challenges, the commercial application of GSNs in dye–wastewater treatment would be successfully realized.

Acknowledgment

One of the authors, Shamik Chowdhury, gratefully acknowledges the financial support provided by the National University of Singapore for his Doctoral study.

References

[1] M. Solis, A. Solis, H.I. Perez, N. Manjarrez, M. Flores, Process Biochem. 47 (2012) 1723–1748.
[2] A. Srinivasan, T. Viraraghavan, J. Environ. Manage. 91 (2010) 1915–1929.
[3] P. Saha, S. Chowdhury, S. Gupta, I. Kumar, Chem. Eng. J. 165 (2010) 874–882.
[4] H.S. Rai, M.S. Bhattacharyya, J. Singh, T.K. Bansal, P. Vats, U.C. Banerjee, Crit. Rev. Environ. Sci. Technol. 35 (2005) 219–238.
[5] V. Augugliaro, M. Bellardita, V. Loddo, G. Palmisano, L. Palmisano, S. Yurdakal, J. Photochem. Photobiol., C: Photochem. Rev. 13 (2012) 224–245.
[6] D. Sud, P. Kaur, Crit. Rev. Environ. Sci. Technol. 42 (2012) 2365–2407.
[7] J.L. Wang, L.J. Xu, Crit. Rev. Environ. Sci. Technol. 42 (2012) 251–325.
[8] M.N. Chong, B. Jin, C.W.K. Chow, C. Saint, Water Res. 44 (2010) 2997–3027.
[9] S. Ahmed, M.G. Rasul, W.N. Martens, R. Brown, M.A. Hashib, Water, Air, Soil Pollut. 215 (2011) 3–29.
[10] L. Han, P. Wang, S. Dong, Nanoscale 4 (2012) 5814–5825.
[11] N. Zhang, Y. Zhang, Y.-J. Xu, Nanoscale 4 (2012) 5792–5813.
[12] R. Leary, A. Westwood, Carbon 49 (2011) 741–772.
[13] Y. Chen, B. Zhang, G. Liu, X. Zhuang, E.-T. Kang, Chem. Soc. Rev. 41 (2012) 4688–4707.
[14] S. Chowdhury, R. Balasubramanian, Adv. Colloid Interface Sci. 204 (2014) 35–56.
[15] M.D. Stoller, S. Park, Y. Zhu, J. An, R.S. Ruoff, Nano Lett. 8 (2008) 3498–3502.
[16] K.I. Bolotin, K.J. Sikes, Z. Jiang, M. Klima, G. Funderberg, J. Hone, P. Kim, H.L. Stormer, Solid State Commun. 146 (2008) 351–355.
[17] A.A. Balandin, S. Ghosh, W. Bao, I. Cailzo, D. Teweldebrhan, F. Miao, C.N. Lau, Nano Lett. 8 (2008) 902–907.
[18] C. Lee, X. Wei, J.W. Kysar, J. Hone, Science 321 (2008) 385–388.
[19] Y. Zhu, S. Murali, W. Cai, X. Li, J.W. Suk, J.R. Potts, R.S. Ruoff, Adv. Mater. 22 (2010) 3906–3924.
[20] V. Singh, D. Joung, L. Zhai, S. Das, S.I. Khondaker, S. Seal, Prog. Mater Sci. 56 (2011) 1178–1271.
[21] S. Pei, H.-M. Cheng, Carbon 50 (2012) 3210–3228.
[22] G. Williams, B. Seger, P.V. Kamt, ACS Nano 2 (2008) 1487–1491.
[23] K.C. Kemp, H. Seems, M. Saleh, N.H. Le, K. Mahesh, V. Chandra, K.S. Kim, Nanoscale 5 (2013) 3149–3171.
[24] A. Mills, S. Le Hunte, J. Photochem. Photobiol., A: Chem. 108 (1997) 1–35.
[25] J.-M. Herrmann, Catal. Today 53 (1999) 115–129.
[26] F. Fujishima, T.N. Rao, D.A. Tryk, J. Photochem. Photobiol., C: Photochem. Rev. 1 (2000) 1–21.
[27] K. Rajeshwar, M.E. Osugi, W. Chanmanee, C.R. Chenthamarakshan, M.V.B. Zanoni, P. Kajitvichyanukul, R. Krishnan-Ayer, J. Photochem. Photobiol., C: Photochem. Rev. 9 (2008) 171–192.
[28] E. Casbeer, V.K. Sharma, X.-Z. Li, Sep. Purif. Technol. 87 (2012) 1–14.
[29] T.-T. Lim, P.-W. Yap, M. Srinivasan, A.G. Fane, Crit. Rev. Environ. Sci. Technol. 41 (2011) 1173–1230.
[30] U.I. Gaya, A.H. Abdullah, J. Photochem. Photobiol., C: Photochem. Rev. 9 (2008) 1–12.
[31] Y. Zang, R. Farnood, Appl. Catal., B: Environ. 79 (2008) 334–340.
[32] A.L. Ivanovskii, Russ. Chem. Rev. 81 (2012) 571–605.
[33] V. Georgakilas, M. Otyepka, A.B. Bourlinos, V. Chandra, N. Kim, K.C. Kemp, P. Hobza, R. Zboril, K.S. Kim, Chem. Rev. 112 (2012) 6156–6214.
[34] H. Wang, X. Yuan, Y. Wu, H. Huang, X. Peng, G. Zeng, H. Zhong, J. Liang, M.M. Ren, Adv. Colloid Interface Sci. 195–196 (2013) 19–40.
[35] Y.-p. Zhang, J.-j. Xu, Z.-h. Sun, C.-z. Li, C.-x. Pan, Prog. Nat. Sci.: Mater. Int. 21 (2011) 467–471.
[36] K. Zhou, Y. Zhu, X. Yang, X. Jiang, C. Li, New J. Chem. 35 (2011) 353–359.
[37] Z. Huimin, S. Fang, F. Xinfei, Y. Hongtao, W. Dan, Q. Xie, Chin. J. Catal. 33 (2012) 777–782.
[38] D. Zhao, G. Sheng, C. Chen, X. Wang, Appl. Catal., B: Environ. 111–112 (2012) 303–308.
[39] A.A. Ismail, R.A. Geioushy, H. Bouzid, S.A. Al-Sayari, A. Al-Hajry, D.W. Bahnemann, Appl. Catal., B: Environ. 129 (2013) 62–70.
[40] S. Liu, H. Sun, S. Liu, S. Wang, Chem. Eng. J. 214 (2013) 298–303.
[41] T. Xu, I. Zhang, H. Cheng, Y. Zhu, Appl. Catal., B: Environ. 101 (2011) 382–387.
[42] H. Fan, X. Zhao, J. Yang, X. Shan, L. Yang, Y. Zhang, X. Li, M. Gao, Catal. Commun. 29 (2012) 29–34.
[43] N.P. Herring, S.H. Almahoudi, C.R. Olson, M.S. El-Shall, J. Nanopart. Res. 14 (2012) 1277.
[44] B. Li, T. Liu, F. Wang, Z. Wang, J. Colloid Interface Sci. 377 (2012) 114–121.
[45] M. Ahmad, E. Ahmed, Z.L. Hong, J.F. Xu, N.R. Khalid, A. Elhissi, W. Ahmed, Appl. Surf. Sci. 274 (2013) 273–281.
[46] A. Wei, L. Xiong, L. Sun, Y. Liu, W. Li, W. Lai, X. Liu, L. Wang, W. Huang, X. Dong, Mater. Res. Bull. 48 (2013) 2855–2860.
[47] Z. Gao, J. Liu, F. Xu, D. Wu, Z. Wu, K. Jiang, Solid State Sci. 14 (2012) 276–280.
[48] D. Chen, Y. Li, Y. Chen, Appl. Mech. Mater. 295–298 (2013) 447–451.
[49] S. Chandra, P. Das, S. Bag, R. Bhar, P. Pramanik, Mater. Sci. Eng., B 177 (2012) 855–861.
[50] M. Zhou, J. Yan, P. Cui, Mater. Lett. 89 (2012) 258–261.
[51] X. Wang, H. Tian, Y. Yang, H. Wang, S. Wang, W. Zheng, Y. Liu, J. Alloys Compd. 524 (2012) 5–12.
[52] S. Pan, X. Liu, New J. Chem. 36 (2012) 1781–1787.
[53] X. An, J.C. Yu, F. Wang, C. Li, Y. Li, Appl. Catal., B: Environ. 129 (2013) 80–88.
[54] W. Tao, J. Chang, D. Wu, Z. Gao, X. Duan, F. Xu, K. Jiang, Mater. Res. Bull. 48 (2013) 538–543.
[55] Y. Fu, X. Sun, X. Wang, Mater. Chem. Phys. 131 (2011) 325–330.
[56] Y. Fu, H. Chen, X. Sun, X. Wang, Appl. Catal., B: Environ. 111–112 (2012) 280–287.
[57] J. Xu, Y. Ao, M. Chen, Mater. Lett. 92 (2013) 126–128.
[58] F. Zhou, R. Shi, Y. Zhu, J. Mol. Catal. A: Chem. 340 (2011) 77–82.
[59] T. Ghosh, K.-Y. Cho, K. Ullah, V. Nikam, C.-Y. Park, Z.-D. Meng, W.-C. Oh, J. Ind. Eng. Chem. 19 (2013) 797–805.
[60] R.C. Pawar, D. Cho, C.S. Lee, Curr. Appl. Phys. 13 (2013) S50–S57.
[61] S. Bai, X. Shen, RSC Adv. 2 (2012) 64–98.
[62] H. Wang, J.T. Robinson, G. Diankov, H. Dai, J. Am. Chem. Soc. 132 (2010) 3270–3271.
[63] J. Guo, S. Zhu, Z. Chen, Y. Li, Z. Yu, Q. Liu, J. Li, C. Feng, D. Zhang, Ultrason. Sonochem. 18 (2011) 1082–1090.
[64] X.-h. Meng, X. Shao, H.-y. Li, J. Yin, J. Wang, F.-z. Liu, X.-h. Liu, M. Wang, H.-l. Zhong, Mater. Lett. 105 (2013) 162–165.
[65] J.R. Potts, D.R. Dreyer, C.W. Bielawski, R.S. Ruoff, Polymer 52 (2011) 5–25.
[66] W.L. Suchanek, R.E. Riman, Adv. Sci. Technol. 45 (2006) 184–193.
[67] J. Li, Z. Chen, R.-J. Wang, D.M. Proserpio, Coord. Chem. Rev. 190–192 (1999) 707–735.
[68] H.R. Pant, C.H. Park, P. Pokharel, L.D. Tijing, D.S. Lee, C.S. Kim, Powder Technol. 235 (2013) 853–858.
[69] S. Vijay Kumar, N.M. Huang, N. Yusoff, H.N. Lim, Mater. Lett. 93 (2013) 411–414.
[70] C.L. Wong, Y.N. Tan, A.R. Mohamed, J. Environ. Manage. 92 (2011) 1669–1680.
[71] R.W. Jones, Fundamental Principles of Sol–Gel Technology, The Institute of Metals, London, 1989.
[72] C.J. Brinker, S.W. Scherer, Sol–Gel Science: The Physics and Chemistry of Sol–Gel Processing, Academic Press, New York, NY, 1990.
[73] K. Li, Y. Huang, L. Yan, Y. Dai, K. Xue, H. Guo, Z. Huang, J. Xiong, Catal. Commun. 18 (2012) 16–20.
[74] K. Li, T. Chen, L. Yan, Y. Dai, Z. Huang, H. Guo, L. Jiang, X. Gao, J. Xiong, D. Song, Catal. Commun. 28 (2012) 196–201.
[75] X. Huang, X. Qi, F. Boey, H. Zhang, Chem. Soc. Rev. 41 (2012) 666–686.
[76] K.C. Patil, S.T. Aruna, T. Mimani, Curr. Opin. Solid State Mater. Sci. 6 (2002) 507–512.
[77] R. Rosa, P. Veronesi, C. Leonelli, Chem. Eng. Process.: Process Intensif. 71 (2013) 2–18.
[78] K.C. Patil, S.T. Aruna, S. Ekambaram, Curr. Opin. Solid State Mater. Sci. 2 (1997) 158–165.
[79] K. Rajeshwar, N.R. de Tacconi, Chem. Soc. Rev. 38 (2009) 1984–1998.
[80] Y. Gao, X. Pu, D. Zhang, G. Ding, X. Shao, J. Ma, Carbon 50 (2012) 4093–4101.
[81] H.M.A. Hassan, V. Abdelsayed, A.E.R.S. Khder, K.M. AbouZeid, J. Terner, M.S. El-Shall, S.I. Al-Resayes, A.A. El-Azhary, J. Mater. Chem. 19 (2009) 3832–3837.
[82] N. Remya, J.-G. Lin, Chem. Eng. J. 166 (2011) 797–813.
[83] H. Hu, X. Wang, F. Liu, J. Wang, C. Xu, Synth. Met. 161 (2011) 404–410.
[84] S. Song, W. Gao, X. Wang, X. Li, D. Liu, Y. Xing, H. Zhang, Dalton Trans. 41 (2012) 10472–10476.
[85] T. Lv, L. Pan, X. Liu, T. Lu, G. Zhu, Z. Sun, J. Alloys Compd. 509 (2011) 10086–10091.
[86] Y. Liu, Y. Hu, M. Zhou, H. Qian, X. Hu, Appl. Catal., B: Environ. 125 (2012) 425–431.
[87] A. Barras, M.R. Das, R.R. Devarapalli, M.V. Shelke, S. Cordier, S. Szunerits, R. Boukherroub, Appl. Catal., B: Environ. 130–131 (2013) 270–276.
[88] L. Guardia, S. Villar-Rodil, J.I. Paredes, R. Rozada, A. Martinez-Alonso, J.M.D. Tascon, Carbon 50 (2012) 1014–1024.
[89] T.-D. Nguyen-Phan, V.H. Pham, E.W. Shin, H.-D. Pham, S. Kim, J.S. Chung, E.J. Kim, S.H. Hur, Chem. Eng. J. 170 (2011) 226–232.
[90] P. Gao, J. Liu, D.D. Sun, W. Ng, J. Hazard. Mater. 250–251 (2013) 412–420.
[91] N. Nasuha, B.H. Hameed, A.T.M. Din, J. Hazard. Mater. 175 (2010) 126–132.
[92] P. Bapat, S.K. Nandy, P. Wangikar, K.V. Venkatesh, J. Microbiol. Methods 65 (2006) 107–116.
[93] S. Chowdhury, P. Saha, Biorem. J. 14 (2010) 196–207.
[94] M. Rafatullah, O. Sulaiman, R. Hashim, J. Hazard. Mater. 177 (2010) 70–80.
[95] Z. Zhang, W. Yang, X. Zou, F. Xu, X. Wang, B. Zhang, J. Tang, J. Colloid Interface Sci. 386 (2012) 198–204.
[96] E. Lee, J.-Y. Hong, H. Kang, J. Jang, J. Hazard. Mater. 219–220 (2012) 13–18.
[97] Y.L. Min, K. Zhang, W. Zhao, F.C. Zheng, Y.C. Chen, Y.G. Zhang, Chem. Eng. J. 193–194 (2012) 203–210.
[98] G. Liu, J.-Y. Liao, A. Duan, Z. Zhang, M. Fowler, A. Yu, J. Mater. Chem., A 1 (2013) 12255–12262.
[99] C.H. Kim, B.-H. Kim, K.S. Yang, Carbon 50 (2012) 2472–2481.
[100] C. Hou, Q. Zhang, Y. Li, H. Wang, J. Hazard. Mater. 205–206 (2012) 229–235.
[101] J. Li, S.l. Zhou, G.-B. Hong, C.-T. Chang, Chem. Eng. J. 219 (2013) 486–491.
[102] N.R. Khalid, E. Ahmed, Z. Hong, M. Ahmad, Appl. Surf. Sci. 263 (2012) 254–259.
[103] G. Chen, M. Sun, Q. Wei, Y. Zhang, B. Zhu, B. Du, J. Hazard. Mater. 244–255 (2013) 86–93.
[104] L. Sun, R. Shao, L. Tang, Z. Chen, J. Alloys Compd. 564 (2013) 55–62.
[105] J. Wang, P. Yang, J. Zhao, Z. Zhu, Appl. Surf. Sci. 282 (2013) 930–936.

[106] Y. Cong, M. Long, Z. Cui, X. Li, Z. Dong, G. Yuan, J. Zhang, Appl. Surf. Sci. 282 (2013) 400–407.
[107] H. Lv, X. Shen, Z. Ji, D. Qiu, G. Zhu, Y. Bi, Appl. Surf. Sci. 284 (2013) 308–314.
[108] G.Y. He, J. Huang, W.F. Liu, X. Wang, H.Q. Chen, X.Q. Sun, Mater. Technol. 27 (2012) 278–283.
[109] Y. Ao, P. Wang, C. Wang, J. Hou, J. Qian, Appl. Surf. Sci. 271 (2013) 265–270.
[110] S. Bai, X. Shen, H. Lv, G. Zhu, C. Bao, Y. Shan, J. Colloid Interface Sci. 405 (2013) 1–9.
[111] H. Sun, S. Liu, S. Liu, S. Wang, Appl. Catal., B: Environ. 146 (2014) 162–168.
[112] X. Zhou, T. Shi, J. Wu, H. Zhou, Appl. Surf. Sci. 287 (2013) 359–368.
[113] X. Yin, H. Zhang, P. Xu, J. Han, J. Li, M. He, RSC Adv. 3 (2013) 18474–18481.
[114] X. Zhou, T. Shi, H. Zhou, Appl. Surf. Sci. 258 (2012) 6204–6211.
[115] S. Liu, H. Sun, S. Suvorova, S. Wang, Chem. Eng. J. 229 (2013) 533–539.
[116] S. Bai, X. Shen, X. Zhong, Y. Liu, G. Zhu, X. Xu, K. Chen, Carbon 50 (2012) 2337–2346.
[117] Y. Zhang, J. Tian, H. Li, L. Wang, X. Qin, A.M. Asiri, A.O. Al-Youbi, X. Sun, Langmuir 28 (2012) 12893–12900.
[118] M. Sookhakian, Y.M. Amin, W.J. Basirun, Appl. Surf. Sci. 283 (2013) 668–677.
[119] P. Dong, Y. Wang, B. Cao, S. Xin, L. Guo, J. Zhang, F. Li, Appl. Catal., B: Environ. 132–133 (2013) 45–53.
[120] X. Liu, L. Pan, T. Lv, Z. Sun, C.Q. Sun, J. Colloid Interface Sci. 408 (2013) 145–150.
[121] X. Wang, H. Tian, W. Zheng, Y. Liu, Mater. Lett. 109 (2013) 100–103.
[122] D.-H. Yoo, T.V. Cuong, V.H. Pham, J.S. Chung, N.T. Khoa, E.J. Kim, S.-H. Hahn, Curr. Appl. Phys. 11 (2011) 805–808.
[123] D. Fu, G. Han, Y. Chang, J. Dong, Mater. Chem. Phys. 132 (2012) 673–681.
[124] Z. Xiong, L.L. Zhang, J. Zhang, X.S. Zhao, Nanosci. Nanotechnol.—Asia 2 (2012) 79–89.
[125] M. Ahmad, E. Ahmed, Z.L. Hong, N.R. Khalid, W. Ahmed, A. Elhissi, J. Alloys Compd. 577 (2013) 717–727.
[126] A. Mittal, A. Malviya, D. Kaur, J. Mittal, L. Kurup, J. Hazard. Mater. 148 (2007) 229–240.
[127] D. Zhang, X. Pu, G. Ding, X. Shao, Y. Gao, J. Liu, M. Gao, Y. Li, J. Alloys Compd. 572 (2013) 199–204.
[128] G.S. Anjusree, A.S. Nair, S.V. Nair, S. Vadukumpully, RSC Adv. 3 (2013) 12933–12938.
[129] H. Liu, W.R. Cao, Y. Su, Z. Chen, Y. Wang, J. Colloid Interface Sci. 398 (2013) 161–167.
[130] N.R. Khalid, E. Ahmed, Z. Hong, Y. Zhang, M. Ahmad, Curr. Appl. Phys. 12 (2012) 1485–1492.
[131] N.R. Khalid, Z. Hong, E. Ahmed, Y. Zhang, H. Chan, M. Ahmad, Appl. Surf. Sci. 258 (2012) 5827–5834.
[132] N.R. Khalid, E. Ahmed, Z. Hong, M. Ahmad, Y. Zhang, S. Khalid, Ceram. Int. 39 (2013) 7107–7113.
[133] N.R. Khalid, E. Ahmed, Z. Hong, Y. Zhang, M. Ullah, M. Ahmed, Ceram. Int. 39 (2013) 3569–3575.
[134] N.R. Khalid, E. Ahmed, Z. Hong, L. Sana, M. Ahmed, Curr. Appl. Phys. 13 (2013) 659–663.
[135] J. Wang, P. Wang, Y. Cao, J. Chen, W. Li, Y. Shao, Y. Zheng, D. Li, Appl. Catal., B: Environ. 136–137 (2013) 94–102.
[136] G. Jiang, Z. Lin, C. Chen, L. Zhu, Q. Chang, N. Wang, W. Wei, H. Tang, Carbon 49 (2011) 2693–2701.
[137] L.M. Pastrana-Martínez, S. Morales-Torres, A.G. Kontos, N.G. Moustakas, J.L. Faria, J.M. Doña-Rodríguez, P. Falaras, A.M.T. Silva, Chem. Eng. J. 224 (2012) 17–23.
[138] X. Pu, D. Zhang, Y. Gao, X. Shao, G. Ding, S. Li, S. Zhao, J. Alloys Compd. 551 (2013) 382–388.
[139] S. Morales-Torres, L.M. Pastrana-Martínez, J.L. Figueiredo, J.L. Faria, A.M.T. Silva, Appl. Surf. Sci. 275 (2013) 361–368.
[140] Z. Liu, W. Xu, J. Fang, X. Xu, S. Wu, X. Zhu, Z. Chen, Appl. Surf. Sci. 259 (2012) 441–447.
[141] Z. Khan, T.R. Chetia, A.K. Vardhaman, D. Barpuzary, C.V. Sastri, M. Qureshi, RSC Adv. 2 (2012) 12122–12128.
[142] L.M. Pastrana-Martínez, S. Morales-Torres, V. Likodimos, J.L. Figueiredo, J.L. Faria, P. Falaras, A.M.T. Silva, Appl. Catal., B: Environ. 123–124 (2012) 241–256.
[143] C. Wang, J. Zhou, L. Chu, J. Liu, Adv. Mater. Res. 662 (2013) 163–166.
[144] W. MingYan, H. JunRao, T. ZhiWei, L. WeiHua, C. Jun, J. Alloys Compd. 568 (2013) 26–35.
[145] S. Sarkar, D. Basak, Chem. Phys. Lett. 561–562 (2013) 125–130.
[146] J. Guo, B. Jiang, X. Zhang, X. Zhou, W. Hou, J. Solid State Chem. 205 (2013) 171–176.
[147] R. Huang, H. Ge, X. Lin, Y. Guo, R. Yuan, X. Fu, Z. Li, RSC Adv. 3 (2013) 1235–1242.
[148] Y. Chen, Y. Tang, S. Luo, C. Liu, Y. Li, J. Alloys Compd. 578 (2013) 242–248.
[149] G. He, M. Qian, X. Sun, Q. Chen, X. Wang, H. Chen, Powder Technol. 246 (2013) 278–283.
[150] L.M. Pastrana-Martíneza, S. Morales-Torresa, S.K. Papageorgioub, F.K. Katsarosb, G.E. Romanosb, J.L. Figueiredoa, J.L. Fariaa, P. Falarasb, A.M.T. Silva, Appl. Catal., B: Environ. 142–143 (2013) 101–111.
[151] Y. Zhang, Z. Chen, S. Liu, Y.-J. Xu, Appl. Catal., B: Environ. 140–141 (2013) 598–607.
[152] A. Di Paola, E. Garcia-Lopez, G. Marci, L. Palmisano, J. Hazard. Mater. 211–212 (2012) 3–29.
[153] K. Nakata, A. Fujishima, J. Photochem. Photobiol., C: Photochem. Rev. 13 (2012) 169–189.
[154] K. Nakata, T. Ochiai, T. Murakami, A. Fujishima, Electrochim. Acta 84 (2012) 103–111.
[155] G. Luo, X. Jiang, M. Li, Q. Shen, L. Zhang, H. Yu, ACS Appl. Mater. Interfaces 5 (2012) 2161–2168.
[156] R. Jain, M. Mathur, S. Sikarwar, A. Mittal, J. Environ. Manage. 85 (2007) 956–964.
[157] J.N. Tiwari, K. Mahesh, N.H. Le, K.C. Kemp, R. Timilsina, R.N. Tiwari, K.S. Kim, Carbon 56 (2013) 173–182.
[158] T.A. Khan, S. Dahiya, I. Ali, Appl. Clay Sci. 69 (2012) 58–66.
[159] Z. Gao, N. Liu, D. Wu, W. Tao, F. Xu, K. Jiang, Appl. Surf. Sci. 258 (2012) 2473–2478.
[160] X. Tu, S. Luo, G. Chen, J. Li, Chem.—Eur. J. 18 (2012) 14359–14366.
[161] Y. Min, F.-J. Zhang, W. Zhao, F. Zheng, Y. Chen, Y. Zhang, Chem. Eng. J. 209 (2012) 215–222.
[162] Q. Zhang, C. Tian, A. Wu, T. Tan, L. Sun, L. Wang, H. Fu, J. Mater. Chem. 22 (2012) 11778–11784.
[163] Z. Qianqian, B. Tang, H. Guoxin, J. Hazard. Mater. 198 (2011) 78–86.
[164] K. Li, J. Xiong, T. Chen, L. Yan, Y. Dai, D. Song, Y. Lv, Z. Xeng, J. Hazard. Mater. 250–251 (2013) 19–28.
[165] J. Hou, C. Yang, Z. Wang, S. Jiao, H. Zhu, Appl. Catal., B: Environ. 129 (2013) 333–341.
[166] F. Xu, Y. Yuan, D. Wu, M. Zhao, Z. Gao, K. Jiang, Mater. Res. Bull. 48 (2013) 2066–2070.
[167] W. Huang, Z. Shu, J. Shi, Catal. Commun. 33 (2013) 24–28.
[168] Z. Xiong, L.L. Zhang, J. Ma, X.S. Zhao, Chem. Commun. 46 (2010) 6099–6101.
[169] F. Wang, K. Zhang, J. Mol. Catal. A: Chem. 345 (2011) 101–107.
[170] T.-D. Nguyen-Phan, V.H. Pham, H. Kweon, J.S. Chung, E.J. Kim, S.H. Hur, E.W. Shin, J. Colloid Interface Sci. 367 (2012) 139–147.
[171] D. Wang, X. Li, J. Chen, X. Tao, Chem. Eng. J. 198–199 (2012) 547–554.
[172] M. Shi, J. Shen, H. Ma, Z. Li, X. Lu, N. Li, M. Ye, Colloids Surf., A: Physicochem. Eng. Aspects 405 (2012) 30–37.
[173] H. Ma, J. Shen, M. Shi, X. Lu, Z. Li, Y. Long, N. Li, M. Ye, Appl. Catal., B: Environ. 121–122 (2012) 198–205.
[174] X. Li, T. Zhang, S. Gu, S.-Z. Kang, G. Li, J. Mu, Sep. Purif. Technol. 108 (2013) 139–142.
[175] P. Wang, Y. Ao, C. Wang, J. Hou, J. Qian, Carbon 50 (2012) 5256–5264.
[176] H.R. Pant, B. Pant, H.J. Kim, A. Amarjargal, C.H. Park, L.D. Tijing, E.K. Kim, C.S. Kim, Ceram. Int. 39 (2013) 5083–5091.
[177] S. Ghasemi, S. SetayeshRahman, A. Habibi-Yangjeh, M.R. Hormozi-Nezhad, M.R. Gholami, J. Hazard. Mater. 199–200 (2012) 170–178.
[178] S. Ghasemi, A. Esfandiar, S.R. Setayesh, A. Habibi-Yangjeh, A. Irajizad, M.R. Gholami, Appl. Catal., A 462–463 (2013) 82–90.
[179] S. Ameen, H.-K. Seo, M.S. Akhtar, H.S. Shin, Chem. Eng. J. 210 (2012) 220–228.
[180] X. Zhang, X. Chang, M.A. Gondal, B. Zhang, Y. Liu, G. Ji, Appl. Surf. Sci. 258 (2012) 7826–7832.
[181] P. Muthirulan, C.K.N. Devi, M.M. Sundaram, Adv. Mater. Lett. 5 (2014) 163–171.
[182] J. Liu, L. Liu, H. Bai, Y. Wang, D.D. Sun, Appl. Catal., B: Environ. 106 (2011) 76–82.
[183] L. Liu, J. Liu, D.D. Sun, Catal. Sci. Technol. 2 (2012) 2525–2532.
[184] S. Ameen, M.S. Akhtar, H.-K. Seo, H.S. Shin, Mater. Lett. 100 (2013) 261–265.